

PRODUCTION OF THE HIGH ENERGY-MOMENTUM SPECTRA OF QUASARS 3C 279 AND 3C 273 USING THE PENROSE MECHANISM

Reva Kay Williams

Department of Astronomy, University of Florida, Gainesville, FL 32611

revak@astro.ufl.edu

ABSTRACT

Theoretical and numerical (Monte Carlo) *N-particle* computer model simulations show that Penrose Compton scattering (PCS) near the event horizon and Penrose pair production (PPP) at or near the photon orbit, in the ergosphere of a supermassive ($M = 10^8 M_\odot$) rotating black hole, can generate the necessary energy-momentum spectra to explain the origin of the mysterious fluxes of ultrarelativistic electrons, inferred from observations to emerge from the cores of Quasars 3C 279 and 3C 273, and other active galactic nuclei (AGNs). Particles from an accretion disk surrounding the black hole fall into the ergosphere and scatter off particles that are in trapped or bound unstable orbits. The Penrose mechanism allows rotational energy of a Kerr black hole, and energy-momentum produced by its strong gravitational field, to be extracted by scattered particles escaping from the ergosphere to infinity (i.e., large distances from the black hole). The results of these model calculations show that the Penrose mechanism is capable of producing the observed high energy particles (\sim GeV) emitted by quasars and other AGNs. This mechanism can extract hard X-ray/ γ -ray photons from PCS of initially infalling low energy UV/soft X-ray photons by target orbiting electrons in the ergosphere. The PPP ($\gamma\gamma \rightarrow e^-e^+$) allows the escape of relativistic e^-e^+ pairs—produced by infalling low energy photons interacting with highly blueshifted target photons at the photon orbit. These e^-e^+ pairs emerge with maximum Lorentz factor $\sim 10^4$, which are consistent with relativistic beaming models used to explain the high energy spectra of so-called blazars, such as 3C 279. Moreover, and importantly, the emission of scattered particles by this mechanism naturally produces relativistic jets collimated about the polar axis, and in most cases one-sided or asymmetrical, agreeing with observations of AGNs. In these fully relativistic calculations, the energy-momentum four vectors (or four-momenta) of the scattered particles are obtained. Based on the consistency of the four-momenta of the scattered Penrose particles with observations of quasars and other objects we observe to be powered by black holes, i.e., the high energies and luminosities, asymmetrical and collimated jets, it appears that the geodesic treatment of many individual particles is sufficient to describe the “flow” of the particles, at least very close to the event horizon.

Subject headings: black hole physics — quasars: individual: (3C 279, 3C 273) — galaxies: nuclei — galaxies: jets — galaxies: active

1. INTRODUCTION

Blazars [optically violently variable (OVV) quasars and BL Lac objects] are probably “normal” active galactic nuclei (AGNs) with relativistic jets pointed somewhat in the direction of the observer, in which Doppler-boosted radiation plays a large part in their observed spectra. Many of the popular models of blazars involve relativistic beaming (Blandford, McKee, & Rees 1977; Cohen et al. 1977; Bassani & Dean 1981; Unwin et al. 1989; Dermer, Schlickeiser, & Mastichiadis 1992; Maraschi, Ghisellini, & Celotti 1992; Dermer & Schlickeiser 1993; Zdziarski & Krolik 1993; Sikora, Begelman, & Rees 1994). These models can explain (1) how the relativistic expansion of the jets avoids electron-positron (e^-e^+) pair production that attenuates γ -rays in compact sources (Bassani & Dean 1981; Dermer et al. 1992) and (2) how the expansion avoids the so-called Compton catastrophe that raises radio photons to X-ray photons by self-Compton scattering (i.e., the expansion provides the conditions for us to observe large fluxes of γ -rays and radio photons). In addition, these models appear to give an explanation for the observed one-sided jets, while also explaining why matter appears to be ejected with speeds greater than the speed of light (superluminal motion). Such models are no doubt important. However, these models are less successful in explaining the origin of the ultrarelativistic electrons emerging from the nucleus with Lorentz factors up to $\gamma \sim 10^4$. Such high energy particles it appears are needed in relativistic beaming models to initiate the expansion. That is, one must first find a mechanism to create copious ultrarelativistic electrons with maximum Lorentz factors $\gamma_{\max} \sim 5 - 7 \times 10^3$ (Sikora, Begelman, & Rees 1994) in order to make these superluminal expansion models operate efficiently to reproduce the observed spectra. Here in this paper, I present such a mechanism.

In this paper, I present a 4-dimensional, fully relativistic, theoretical and numerical (Monte Carlo) model calculation of Penrose (1969) scattering processes in the ergosphere of a supermassive rotating black hole, which allows the extraction of orbital energy and momentum from particles in bound trapped orbits near the event horizon. This energy and momentum escape from the black hole to large distances in the form of X-rays, γ -rays, and e^-e^+ pairs. This black hole model for the energy source of AGNs (1) naturally produces one-sided jets—a purely relativistic effect related to the extreme inertial frame dragging in the ergosphere (Williams 2002a, 2002b, 2001); (2) shows that AGNs may or may not be strong γ -ray emitters, depending on the form of the accretion disk and the jet axis orientation relative to the observers line of sight; (3) e^-e^+ pairs emerge from the nucleus with Lorentz factors up to $\sim 10^5$, enabling relativistic beaming models to yield apparent energies in the TeV range; and (4) produces jets of escaping energetic vortical orbiting particles collimated about the rotation axis of the black hole (de Felice & Carlotto 1997; Williams 2002b,

2001)—this also is a purely relativistic effect caused by the frame dragging. This frame dragging (sometimes referred to as the Lense-Thirring effect) is due to the gravitational force associated with a rotating mass (Thirring & Lense 1918).

In general, past models have attempted to explain both items (1) and (2) above solely by relativistic beaming; and because of this, inconsistencies have arisen: observations seem to suggest that these features (the one-sided jets and the sometimes strong γ -ray emission) may not just be optical illusions, as in the case of relativistic beaming models, but instead may also be intrinsic to the source (Barthel 1987). I have found this to be true in the theoretical and numerical analysis of the Penrose mechanism presented in this paper. In addition, relativistic beaming models can not explain one-sided jets when the observed radiation from the jet does not appear to be near the observer’s line of sight, i.e., when the source exhibits little superluminal expansion (Jones 1987). Moreover, findings by Dennett-Thorpe et al. (1997), after studying the asymmetry of jets, lobe length, and spectral index in a sample of quasars, with well defined jets, led them to conclude that the simplest models of relativistic beaming fail to explain the “present observations”; and that only if the intrinsic spectrum is curved (i.e., with the spectral index increasing with frequency), such that the approaching lobe is seen at a significant lower frequency, will asymmetry of the right sense be produced. This supports my findings that some asymmetry in the jet/counter jet may be intrinsic to the energy source, and that, relativistic beaming may just serve as an important enhancement mechanism (Williams 2002a, 2002b). Further, observations of so-called microquasars in our Galaxy show some asymmetry in the jet and counter jet distributions (Mirabel & Rodriguez 1998); and not all of the observed asymmetry can be explained by relativistic beaming, suggesting that some asymmetry is intrinsic (Hjellming & Rupen 1995; Mirabel & Rodriguez 1996).

As related to item (3) above, some attempts have been made to generate the ultrarelativistic particles in standard accretion disk models using electrodynamics (Blandford 1976, Blandford & Znajek 1977; Macdonald & Thorne 1982; Phinney 1982; Blandford & Payne 1982; Lovelace 1976, Lovelace & Scott 1982; Lovelace & Burns 1982; Punsly & Coroniti 1989, 1990a, 1990b; Punsly 1991). In such models, it is proposed that, the dipolar-like magnetic field lines—due to the accretion disk—thread through the highly conductive disk plasma, inducing an electric field while torquing the rotating black hole or the accretion disk, creating an electromagnetic field which acts like a dynamo, resulting in the generation of two oppositely-directed jets of Poynting fluxes [$\sim c/4\pi(\mathbf{E} \times \mathbf{B})$] of electromagnetic energy. These past models are complex and have problems as pointed out by Punsly and Coroniti (1989, 1990a, 1990b). The model (Punsly 1991) in which the disk magnetic field lines thread the ergospheric disk, extracting rotational energy by means of magnetohydrodynamics (MHD), although complex, appears to be potentially powerful; however, it in itself, does not appear to produce the large Lorentz factors and luminosities needed to universally explain observations. Moreover, such models, as of yet, are not easy to qualify (Eilek 1980, 1991), even until today. The electrodynamics of these models probably best describe collimation and acceleration of relativistic particles that emerge from the nucleus by some other process, such as the Penrose process described here; and thus, the electrodynamics could possibly sustain the jets of relativistic particles out to

their observed distances, while producing the beaming effect.

Now, it has been generally believed in the past that inflow from the accretion disk into the black hole is a MHD (or hydrodynamic) process; and one would think that postulating particles in geodesic orbits is inconsistent with participating in the inflow. However, these present model calculations are not saying that the Penrose scattering particles do not participate in the inflow—yielding inconsistency; what they are saying is that the geodesic characteristics of the particles appear to be the best way to define the inflow and outflow of plasma close to the event horizon. This flow, of course, can no doubt be treated as a fluid: whose velocity pattern is controlled by the density, pressure, temperature, magnetic field, and gravitational field—however, MHD may not be the best treatment for this already extremely complex problem, i.e., where gravity is dominant.

Moreover, based on the consistency of the energy-momentum four-vectors (or four-momenta) of the scattered Penrose particles with the observations of quasars and other objects we observe to be powered by black holes (i.e., high energies and luminosities, asymmetrical and collimated jets), it appears that the geodesic treatment of many individual particles is sufficient to describe the flow, at least very close to the event horizon. At most, MHD models (whenever the major problems associated with them are worked out, such as, how to convert from electromagnetic energy to particle energy, i.e., from a Poynting flux to a relativistic particle flux) will duplicate what I have already found from these Penrose processes (see for example the discussing in Appendix A), and will in no doubt describe the flow of the jets away from the black hole, at a distance where electromagnetic collimation due to accretion disk properties may become important. However, the single-particle approach is essential close to the black hole even in a more realistic MHD treatment, especially when the fluid is in a supersonic regime (de Felice & Carlotto 1997). Gravity apparently causes the bulk of fluid elements to behave like the bulk motion of individual particles moving along geodesics.

Further, considering the Blandford-Znajek (1977) model referenced above, although recently, once again, has risen in popularity, this model which attempts to extract rotational energy from a rotating black hole, as related to the Penrose mechanism, is not tenable, as pointed out by Punsly and Coroniti (1989, 1990a, 1990b), according to the “no-hair” theorem (Carter 1973; Misner, Thorne, & Wheeler 1973) and the “vacuum infinity” horizon (Regge & Wheeler 1957; Punsly 1989). Specifically, the Blandford-Znajek model appears to be untenable for at least two reasons: (1) it relies on energy and angular momentum being transported out of the event horizon by an electric current; however, the assumption that the electric current can freely flow into and out of the horizon is not valid; (2) the horizon is causally decoupled from the accretion disk plasma, including its magnetic field, thus making this model an ineffective way of extracting rotational energy (Punsly 1991, 1996). In other words, the magnetic field lines of the surrounding accretion disk cannot anchor to the “vacuum infinity,” and in general, charge neutral horizon, before being expelled or redshifted away (Bičák 2000; Bičák & Ledvinka 2000), thereby being unable to torque the black hole, generating an electric field, leading to a Poynting flux. That is, just as the Kerr metric (§ 2) asymptotically goes to a Minkowski (flat spacetime) metric at infinity, such that an

observer at infinity is not affected by the black hole, so is the vacuum infinity horizon to the magnetic field and neutral plasma of the accretion disk, suggesting that Blandford-Znajek type models may be important at an “effective” faraway distance from the event horizon. This presents a problem for MHD models of AGNs that rely on the Blandford-Znajek process to extract electromagnetic energy from the rotating black hole (e.g., Blandford & Levinson 1994; Hirotani & Okamoto 1998; Li 2002).

Still other attempts have been made to create the ultrarelativistic electrons by shocks in the jets themselves, associated with either dense clouds accelerated by the flow or with an unsteady velocity field in the jet (Blandford & McKee 1977; Jones & Tobin 1977; Marscher 1978). Such shocks could possibly explain the local acceleration along the jet at a distance from the nucleus, perhaps even out to the lobes. However, these models are not self-contained; they must assume that the initial blast, which initiates the shocks, originated within the nucleus of the compact source as a result of an explosion or instability.

In this paper, I present an analysis of the Penrose mechanism by which the central black hole source can eject a “blast” of ultrarelativistic particles, escaping into the polar regions, mainly e^-e^+ pairs and some lower energy hard X-ray and γ -ray photons. Subsequently, the Penrose produced pairs can possibly interact with a surrounding electromagnetic field, through synchrotron and curvature radiation processes, while undergoing Comptonization, thereby, adding to the initial Penrose relativistic expansion, and thus, giving rise to shock waves and beaming effects.

The Penrose mechanism, or black hole model for AGNs, presented here, invokes the ultrarelativistic e^-e^+ pair production as a direct result of the high temperatures in the accretion disk. Shapiro, Lightman, and Eardley (1976) and other authors (Eilek 1980; Eilek and Kafatos 1983) calculate a model for a two-temperature disk in which the protons in the inner region of the disk attain a temperature of $\sim 2 \times 10^{12}$ K due to the absence of any efficient cooling mechanism (see § 4.1 for details). Such high temperatures ($k_B T \sim 200$ MeV) can result in copious pion production (Eilek 1980; Mahadevan, Narayan, & Krolik 1997), in which neutral pion (π^0) decays, produce abundant γ -rays with energies up to ~ 100 MeV, narrowly peaked around ≈ 75 MeV, assuming that the initial protons have a thermal distribution. Such decay products are candidates for the Penrose mechanism. Williams (1995, hereafter Paper 1) has shown that Penrose pair production (PPP), in the ergosphere of a supermassive ($10^8 M_\odot$) rotating Kerr black hole (KBH), at the photon orbit, can be significant, wherein, the γ -rays, resulting from π^0 decays, are used as seed photons to populate the photon orbit. Moreover, such accretion disks with thermally unstable inner regions (Piran 1978), which could vary between unstable configurations (Narayan 1997), would be conducive to a blast of ultrarelativistic particles.

Eilek and Kafatos (1983) used the structure of the two-temperature disk in a canonical Kerr metric (Thorne 1974) to calculate the high-energy spectrum of such disks. They predict γ -ray luminosity, due to the π^0 decays, as high as 10% of the bolometric luminosity in sub-Eddington models. In these present calculations, I assume such γ -ray luminosity [calculated to be $\sim 10^{43}$ erg s $^{-1}$ at

$\sim 75\text{--}100$ MeV, yielding a γ -ray rate of $\sim 7 \times 10^{46} \text{ s}^{-1}$ (Eilek & Kafatos 1983)] to populate the photon orbit in the highest energy PPP ($\gamma\gamma \rightarrow e^-e^+$) processes. These infalling γ -rays are assumed to populate the photon orbit by a method similar to that assumed by Eilek and Kafatos (1983), and earlier by Leiter and Kafatos (1978), to supply the seed photons for PPP ($\gamma p \rightarrow e^-e^+p$) in the Coulomb field of orbiting protons near the event horizon, specifically between the radii of marginally bound r_{mb} and marginally stable r_{ms} orbits. Such seed photons, proposed by these authors, after being blueshifted in energy by a factor of ~ 30 (see below), due to rotation of the KBH and the curvature of spacetime, will achieve energies as high as \sim GeV. However, it is shown in Paper 1 that the PPP ($\gamma p \rightarrow e^-e^+p$) in the Coulomb field of a proton as initially proposed by Leiter and Kafatos (1978), proved to be unfruitful (see discussion in § 2). Nevertheless, it is also shown in Paper 1, that, when these γ -rays (produced by the π^0 decays) are assumed to populate the photon orbit, upon being blueshifted in energy by a factor of ~ 52 (see below), the PPP ($\gamma\gamma \rightarrow e^-e^+$) can occur in which large fluxes of ultrarelativistic e^-e^+ pairs of energy \sim GeV are allowed to escape from the nucleus into the polar regions. An aim of this paper is to show that such ultrarelativistic PPP electrons (with $\gamma \sim 10^4$) can undergo inverse Comptonization with surrounding lower energy photons, say from the accretion disk, boosting the energy of these photons up to \sim GeV, or apparently higher due to beaming effects, and the resulting γ -ray luminosities are consistent with the observed spectra of quasars 3C 279 and 3C 273.

Note, the blueshift factor $e^{-\nu}$, mentioned above, can be found in the transformation Eq. (2.8d) of Paper 1, and is given by the Kerr metric coefficient Eq. (2.10a), also of Paper 1. It is a well known parameter in the theory of Kerr metric black holes. Its inverse is sometimes referred to as the "redshift factor" (Thorne et al. 1986; see also Eq. (2.7d) of Paper 1). This blueshift factor gives the blueshift in the energy of a particle, at a specific radius, as measured by a local frame observer. Such blueshifted energies of the particles (due to the fact that any particle falling into the ergosphere must rotate in the direction of the KBH) can be extracted by these Penrose scattering processes (as will be described in this paper). The calculated values of the blueshift factors at the radii r_{ms} , r_{mb} , and r_{ph} , the photon orbit, are approximately 10.7, 32, and 52, respectively, for $a = 0.998M$ (where a is the angular momentum per unit mass parameter of the KBH, with $G = c = 1$),

In general, the observed spectra of quasars show intense nonthermal continuum radiation with highly excited emission lines. The broad-band photon spectrum shows a characteristic mixture of thermal and nonthermal emission, from radio to γ -ray frequencies. The nonthermal continuum spectrum appears to be associated with the nucleus and the astrophysical jets, and the thermal emission appears to be associated with the accretion disk. Features in the radio, X-ray, and γ -ray spectra, and the astrophysical jets associated with radio loud quasars seem to distinguish two populations: radio loud and radio quiet quasars. For example, in radio loud quasars, the infrared baseline power law that always drops in the millimeter band (the mm-break) drops only ~ 2 decades. The great majority of quasars, i.e., the radio quiet quasars, have a much stronger mm-break ~ 5 to 6 decades (Elvis 1988). The size of the mm-break does not seem to affect the infrared (IR) to UV

continuum shapes. However, there is clearly a correlation between radio loudness and the X-ray emission slope: a weak mm-break implies a strong X-ray turn up. Moreover, observations (Fichtel 1992, 1993) suggest that the high energy γ -ray spectra ($\gtrsim 30$ MeV) detected in radio loud quasars further distinguish the two populations, since only radio loud quasars were detected in this energy range. In this paper, I show that the density and thermal instabilities occurring in the inner region of the accretion disk [which increase the temperature, giving rise to the so-called two-temperature, bistable disk model, in which the disk can in principle exist in two phases: a thin disk and ion torus (Lightman & Eardley 1974; Shapiro, Lightman, & Eardley 1976)] could be closely related to there being radio loud and radio quiet quasars. Disk models of this sort are also referred to as thin disk/ion corona models, or more recently, the “hot” phase of these type of disks have been called advection dominated accretion flows (ADAFs): further details are given in § 4. In ADAFs, the energy released by viscous dissipation is stored in the gas as entropy and advected into the black hole with a small fraction being radiated away (Narayan & Yi 1994, 1995; Narayan, Kato, Honma 1997; Narayan et al. 1998). Note that, I will sometimes interchangeably refer to the ion corona as the ion torus or ADAF.

Energies as high as $\sim 4 - 10$ GeV have been observed in the spectral observations of quasars 3C 279, 3C 273, PKS 0208–512, and PKS 0528+134 (Hartman et al. 1992; von Montigny et al. 1993; Hermsen et al. 1993; Hunter et al. 1993). Even higher energies \sim TeV have been observed in the BL Lac γ -ray source Markarian 421 (Punch et al. 1992; Zdziarski & Krolik 1993). Figure 1 shows schematic energy spectra of 3C 279 and 3C 273, based on a number of observations. Details of Figure 1 will be discussed in later sections of this paper.

Overall, in this paper, I present results of theoretical model calculations using the Monte Carlo numerical method to treat Penrose scattering processes in the ergosphere of a KBH: the cases considered here are inverse Compton scattering and γ -ray— γ -ray pair production ($\gamma\gamma \rightarrow e^-e^+$). These processes are assumed to occur in material falling into the ergospheric region of a rotating black hole from a surrounding accretion disk that extends inside the ergosphere to approximately the marginally stable radius (Eilek 1980). Resulting from these scattering processes, high energy particles are emitted with calculated luminosities that are in agreement with the general observed spectra of AGNs; and in this model, relativistic beaming can be used as an enhancement mechanism, giving rise to the objects we call blazars. The theoretical background for these computations are presented in Paper 1 (I refer the reader to Paper 1 for a thorough description of the model). Here, I concentrate on the astrophysical results, using these Penrose processes to explain the observed energy spectra of 3C 279 and 3C 273: these quasars were chosen because of the availability of the data on them, while assuming that they can serve to represent in general all AGNs. In § 2, a summary is given of the general formalism of the Penrose mechanism considered in Paper 1. In § 3, relevant observations of 3C 279, 3C 273, and other AGNs are presented. In § 4, I summarize the overall results of the Penrose Compton scattering (PCS) and PPP processes considered in Paper 1. This summary includes an astrophysical discussion of the PCS and PPP ($\gamma\gamma \rightarrow e^-e^+$) processes, as correlated with popular theoretical accretion disk models for AGNs, in particular the classical

thin disk and the thin disk/ion corona. In § 5, I compare the model results with observations of 3C 279 and 3C 273. Specifically, I compare the observed luminosity spectra with the calculated luminosity spectra due to the Penrose processes. Finally, in § 6, I present conclusions and future investigations.

2. THE PENROSE PROCESS

A mechanism suggested by Roger Penrose (1969) permits rotational energy to be extracted from a KBH. The *classical* Penrose process utilizes the existence of retrograde particle orbits (with respect to the rotation of the KBH) in the ergosphere. In general, it is possible for a particle, say p_1 , that has fallen inwardly from infinity into the ergosphere to scatter off another particle, say p_2 , initially in a bound direct orbit. If the orbit of the scattering particle p_2 changes into a retrograde orbit (of negative energy), then the scattered particle p_1 can escape to infinity with more mass-energy than the sum of the initial energies of p_1 and p_2 . Since the orbit of the initially bound particle p_2 is dependent on the angular momentum of the KBH and the curvature of spacetime defined by the mass M of the black hole, then, consequently, when p_2 gives up energy to the escaping particle p_1 and falls through the event horizon, the KBH loses energy in the form of rotational energy. A possible class of Penrose processes occur when particles already inside the ergosphere (say particles from an accretion disk) undergo local relativistic scatterings (Piran, Shaham, & Katz 1975; Paper 1). If one of the scattering particles is initially in a bound orbit, as in the general description above, then it is possible for the other initially unbound scattered particle to escape to infinity with rotational energy from the KBH. This process allows scattered ergospheric particles to (1) escape to infinity with more mass-energy than they would have had if the scattering occurred outside the ergosphere; and (2) escape to infinity with mass-energy initially trapped by the KBH, mass-energy that more than likely had no other way of escaping, save these Penrose processes. This is because for a particle initially trapped by the KBH, an escaping orbit is said to occur only when some physical process near the hole injects the particle into such an orbit (Bardeen, Press, & Teukolsky 1972).

Since the inner edge of an accretion disk around a KBH with $a \gtrsim 0.95M$ can extend inward to the radius of marginal stable orbits, $r_{\text{ms}} \simeq 1.2M$, which is inside the ergosphere, then a large enough fraction of the disk luminosity can possibly reach the radii of importance for the occurrences of Penrose scattering processes. That is, the fraction of the disk luminosity intersecting at the the scattering radii will be larger than for the case in which the accretion disk does not extend inside the ergosphere, such as in the cases of nonrotating ($a=0$) and slow rotating black holes.

An expression for the fraction of the disk luminosity that falls onto the scattering radii of the black hole can be found. We assume that the disk can be represented by cylindrical surfaces of various radii r , concentric about a spherical shaped region representing near the event horizon of the black hole. An element of area representing the disk at a given radius $r = r_d$, centered on the

black hole, as measured by an observer at infinity, can be expressed as

$$da_d = r_d d\Phi dZ, \quad (1)$$

where r_d is the inner radius of the disk. Similarly, an element of area at the scattering radius r_s on the surface of the sphere representing the region near the black hole is given by

$$da_s = r_s^2 \sin \Theta d\Phi d\Theta. \quad (2)$$

We assume also that the disk, which extends inside the ergosphere, radiates into the volume element of space $\sim (r_d^2 - r_s^2) d\Phi dZ$, for sufficiently small dZ and $r_s \sim r_d$, such that the flux of the radiation from the disk remains nearly constant inward to the scattering radii. The above assumptions allow an expression for the photon luminosity intersecting the scattering radii:

$$L_s \approx \frac{r_s^2}{r_d h} (\cos \theta_1 - \cos \theta_2) L_\gamma, \quad (3)$$

where L_γ is the disk photon luminosity at the cylindric surface of radius r_d and height $h/2$ above and below the equatorial plane. Equation (3) gives the fraction of the disk luminosity impinging on a solid angle with polar bandwidth $\Delta\theta = \theta_2 - \theta_1$ subtended the black hole at the scattering radius r_s , where θ_1 and θ_2 are polar angles above and below the equatorial plane. From equation (3), we see that θ_1 and θ_2 can be used as free parameters in these model calculations, however, within limits, as explained below.

Note, equation (3), only gives a fraction (or probability), and, therefore, the “strong bending” of photon trajectories need not be considered here, since this fraction is only used to show what is needed to fit the model calculated luminosity, due to the Penrose mechanism, with observations (see § 5). That is, the calculated Penrose luminosity assumes that every particle in L_γ scatters; the fraction given by equation (3) in part accounts for this unrealistic assumption, since in a realistic situation we know that only a fraction of the particles will scatter.

Now, the luminosity of photons from the disk used to participate in the Penrose scattering processes, defined by L_γ in equation (3), is assumed to be a power law distribution based on spectra observations of 3C 279 and 3C 273 (as described in § 5.1). In the trajectories of the infalling photons, that actually participate in the individual scattering events, the so-called bending of the light or the warping of spacetime by the rotating black hole has been taken into account, since they are assumed to fall radially along null geodesics in the Kerr metric, with the conserved azimuthal angular momentum as measure by an observer at infinity $L = P_\Phi$ set equal to zero. This assumption has also been used by other authors (Piran & Shaham 1977a; Leiter & Kafatos 1978; Kafatos & Leiter 1979) for maximum energy gain in a Penrose scattering process. In a more realistic situation, L will not just be zero, i.e., the incident angle of the photon relative to the motion of the target particle will generally be anywhere from 0° to 90° . (Note, $L=0$ means that the incident angle is 90° .)

If we normalize equation (3) to unity at the inner radius of the accretion disk, by setting $r_s = r_d$ and the luminosity $L_s = L_\gamma$, we get the condition that $(r_d/h)(\cos \theta_1 - \cos \theta_2) \approx 1$. This

puts a constraint on the values of θ_1 and θ_2 . For example, for the two-temperature accretion disk used in these calculations, of say height $h \simeq 0.779M$, normalized to unity at $r_d \simeq 1.3M$ (see § 4.1), it is required that $\theta_1 \gtrsim 73^\circ$, $\theta_2 \lesssim 108^\circ$, implying that $\Delta\theta$ must always be $\lesssim 35^\circ$. If these requirements are satisfied, then equation (3) gives that, from $\sim 85\%$ at $r_s \equiv r_{\text{ms}} \simeq 1.2M$ to $\sim 68\%$ at $r_s \equiv r_{\text{ph}} \simeq 1.074M$ of the photons generated in the accretion disk at $r_d = 1.3M$ can fall onto the black hole at these scattering radii (r_s), between $\Delta\theta \approx 35^\circ$. These radii are where the PCS and the PPP ($\gamma\gamma \longrightarrow e^-e^+$) take place. So, we see that, if the accretion disk extends inside the ergosphere ($\simeq 2M$ for $a = 0.998M$), a large enough fraction of the disk luminosity reaches the scattering radii to make the Penrose mechanism a feasible process in the contribution to the observed spectra of AGNs, contrary to what is estimated to occur in reference to the accretion disk being far away from the ergospheric region, where, in this case, only $\sim 1 - 10\%$ (for $r_d \gg r_s$) of the disk luminosity would reach the scattering radii (Eilek & Kafatos 1983).

However, as we shall see in this investigation, the ratio found in equation (3) need not be larger than $L_s/L_\gamma \simeq 4\%$ in order for the Penrose mechanism described here to be an effective energy source for AGNs.

Overall, this Penrose mechanism could very well be the important source of the relativistic particles emerging from the nucleus of quasars and other AGNs. The physical background needed for these Penrose processes to occur is described below.

The Kerr metric (Kerr 1963), a stationary, axially symmetric, asymptotically flat spacetime solution to the vacuum Einstein field equations, describes the geometry outside of a rotating massive body. This metric, conveniently written in the Boyer-Lindquist coordinates (Boyer & Lindquist 1967), defines the spacetime separation between events near a rotating black hole as measured by an observer at infinity—referred to as the Boyer-Lindquist coordinate frame (BLF). The general orbits of particles (including photons) near the KBH are best described in the BLF. The BLF admits three constants of motion as measured by an observer at infinity (Carter 1968). They are the total energy E , the angular momentum parallel to the symmetry axis L , and the “ Q value” given by

$$Q = P_\Theta^2 + \cos^2 \Theta \left[a^2 \left(\mu_o^2 - E^2 \right) + \frac{L^2}{\sin^2 \Theta} \right], \quad (4)$$

where μ_o is the rest mass energy of the particle, which is a trivial fourth constant of motion. The value of Q is zero for particles whose motions are confined to the equatorial plane. The nonzero values of Q belong to particles which are moving in the Θ -direction (i.e., polar direction) and/or are not confined to the equatorial plane.

In general, the parameter a of equation (4) can have values $0 \leq (a/M) \leq 1$, values which allow for the existence of an event horizon. When $a = 0$, the Kerr metric reduces to the form of the Schwarzschild metric for a nonrotating massive body. For definiteness, a canonical KBH is used, with its limiting value $a/M = 0.998$, as defined by Thorne (1974) in his investigation of an accretion disk around a KBH. It is found that, if a/M is initially very close to 1 ($0.999 \leq a/M \leq 1$), a small amount of accretion ($\Delta M/M \leq 0.05$) through a disk quickly spins the hole down to a limiting state

$a/M \simeq 0.998$. Conversely, if a/M is initially below this limiting value, accretion spins the hole up toward it.

Upon approaching a KBH from infinity, a limit or a region is reached where the angular momentum of the KBH causes inertial frames to be dragged around in the direction that the black hole rotates. This means that, it is impossible for an observer inside this so-called stationary limit to remain at rest relative to distant observers. This limit is given analytically by

$$r = r_o = M + \left(M^2 - a^2 \cos^2 \Theta \right)^{1/2}. \quad (5)$$

The region between this stationary limit and the event horizon [located at $r = r_+ = M + \left(M^2 - a^2 \right)^{1/2}$] is called the ergosphere. This means that, inside the ergosphere, the Kerr metric in the BLF does not allow an observer to be stationary (in the sense of the observer being at rest with $r, \Theta, \Phi = \text{constant}$) because of the dragging of inertial frames; this makes physical processes difficult to describe in the BLF. In order to examine physical processes inside the ergosphere, Bardeen, Press, & Teukolsky (1972) devised a frame of reference called the local nonrotating frame (LNRF). Observers in this frame rotate with the KBH in such away that the frame dragging effect of the rotating black hole is canceled as much as possible. In the LNRF, special relativity applies since locally spacetime has Lorentz or flat spacetime geometry. That is, the LNRF is used as a convenient inertial frame to describe physical processes inside the ergosphere—then one must transform back to the BLF to find out what is measured by an observer at infinity (see Paper 1 for details).

Now, of the three Penrose scattering processes presented in Paper 1: PCS, PPP ($\gamma\gamma \rightarrow e^-e^+$), and PPP ($\gamma p \rightarrow e^-e^+p$), the most rewarding ones were the PCS and the PPP ($\gamma\gamma \rightarrow e^-e^+$). These rewarding processes are summarized in details in § 4 of this present paper. Unfortunately, the PPP ($\gamma p \rightarrow e^-e^+p$), as mentioned earlier, as suggested by some authors (Leiter & Kafatos 1978; Kafatos & Leiter 1979; Eilek & Kafatos 1983) did not allow any of the scattered e^-e^+ pairs to escape, mainly because of the large acquired inward radial momenta of the infalling blueshifted incident photons at the scattering radius, too large for the produced pairs to be scattered outward by the protons. This large inward radial momentum arises because of the assumption that the angular momentum L is zero for the infalling incident photons. [Note, $L = 0$ was assumed only for maximum energy gain in a Penrose scattering process. This assumption is not made for the infalling γ -rays, mentioned in § 1, that are assumed to populate the photon orbit in the PPP ($\gamma\gamma \rightarrow e^-e^+$). These γ -rays will indeed acquire large L as well large E .] I refer the reader to Paper 1 for details concerning the PPP ($\gamma p \rightarrow e^-e^+p$).

3. OBSERVATIONS

3.1. General

Since the discovery of quasars in 1963, numerous observations have been made of them and other AGNs. Below I present some of the general observed features that are relevant to the present model calculations. Quasars are observed to be the most distant objects, with redshifts up to $z \sim 5.5$ (Schmidt 1992; Stern et al. 2000). It is generally accepted by the astrophysical community that these objects and other AGNs are powered by massive black holes at their cores. Even before 1994, the year in which NASA’s Hubble Space Telescope began confirming the existence of black holes in the center of numerous galaxies, a large amount of circumstantial evidence for the presence of massive black holes ($M \gtrsim 10^6 M_\odot$) in the nuclei of bright nearby galaxies ($d \leq 20$ Mpc) had accumulated (Filippenko 1988). Further, the overall nuclear activities in galaxies seem to decrease as observational distances approach nearby galaxies. This should be of no surprise if one believes that many nearby galaxies are evolved quasars that have outlived their quasar phases; i.e., their nuclear activities have decreased as the available matter they “feed” off has depleted.

Some observed spectral properties of AGNs are the following: At energies greater than 2 keV, the X-ray spectra of AGNs show a remarkable uniformity with almost all objects, well fixed by simple power laws in the 2 – 100 keV band with narrow dispersion in spectral index $\alpha \sim 0.7 \pm 0.15$, as related to the flux density f_ν of the photons having a power law $k\nu^{-\alpha}$ distribution. This universal X-ray power law also exists in lower mass galactic black hole candidates, which suggests that this feature may be due to processes inherent to the central power source. Moreover, it is generally believed that X-ray emission in radio selected QSOs (quasi-stellar objects) is likely to have two components: one thermal related to the optical luminosity ($\alpha \sim 0.5$), and one nonthermal related to the radio luminosity ($\alpha \sim 0.8$; Isobe et al. 1988). The thermal component could very well be related to the inner region of the accretion disk, and the nonthermal to Penrose processes, as described in § 5.2 of this paper.

AGNs emit the major fraction of their power in the γ -ray region of the electromagnetic spectrum (Bassani et al. 1985). In this region, the observed spectral slopes of quasars range from $1.7 \lesssim \alpha \lesssim 2.6$ (Hartman et al. 1992; Hunter et al. 1993; Bertsch et al. 1993; von Montigny et al. 1993; Hermsen et al. 1993), as in the photon emission power law $N_E = kE^{-\alpha}$. The steep spectra up to $\alpha \simeq 2.6$ may be an indication either that photons with a broad range of spectral index are emitted from quasars or that the photon spectrum is a function of the angle from the jet axis (Hunter et al. 1993), or perhaps a combination of both. Since a large fraction of emitted power is contained at γ -ray energies above ~ 1 MeV, this suggests that the production of the γ -ray photons is intimately related to the central power source. Also, recall that, energies as high as \sim TeV have been observed (Punch et al. 1992; Zdziarski & Krolik 1993).

Observations show AGNs to be variable on time scales ranging from less than an hour (Hartman et al. 1992) up to years. In general, this variability appears to be related to accretion disk

instabilities. Blazars are the most variable AGNs; and they are among the most luminous known objects. From variability studies we know that much of their luminosity is generated inside volumes at most ~ 0.008 pc across (Jones 1988). Because they are linear polarized at several percent, the prevailing view is that the emission is synchrotron. These objects make up only $\sim 2\%$ of all known AGNs. As mentioned earlier, relativistic beaming is believed to be important in these object, wherein we observe an apparent increase in source luminosity and energy, and an apparent decrease in size.

When comparing a number of different AGNs observations (Hermesen et al. 1992; Fichtel 1992; Hunter et al. 1993), there appears to be five universal regions in the luminosity spectrum where energy is definitely emitted: at $\nu \sim 10^{9-12}$ Hz (radio/mm), $\nu \sim 10^{13} - 2 \times 10^{15}$ Hz (infrared/optical/UV), $\nu \sim 10^{17-20}$ Hz (X-ray), $\nu \sim 10^{21-22}$ Hz (soft γ -ray), and $\nu \sim 10^{22-24}$ (γ -ray); compare Figure 1. The exact location of emission, in these regions on the observed luminosity spectrum, probably depends on the characteristics of the accretion disk and to what extent the source is superluminous. The observed \sim TeV emission in Mrk 412 and a few other blazars (Stecker, de Jager, & Salamon 1996) appear, from these present model calculations, to be extreme cases of conditions that can occur to effect the observed spectrum (namely, Penrose processes, relativistic beaming, and an ADAF)—as will be discussed in § 6.

3.2. 3C 279

Quasar 3C 279 (Fig. 1a) is an OVV quasar, which means, in general, that observations show intense optical variability, and a highly polarized optical continuum; 3C 279 is also radio loud. It has a redshift $z = 0.538$, implying a distance $d \simeq cz/H_0 \simeq 2.2 \times 10^3$ Mpc ($H_0 = 75$ km s $^{-1}$ Mpc $^{-1}$). This quasar was the first object in which superluminal motion was detected (Whitney et al. 1971). A change of 20% in X-ray intensity (2 – 20 keV) on a time scale of less than an hour has been observed. In general, the X-ray luminosity is observed to vary around $L_x \sim 10^{46}$ erg s $^{-1}$, with flux f_ν spectral index $\alpha \sim 0.5$ (i.e., photon N_E or N_ν spectral index $\alpha \sim 1.5$). In γ -ray intensity (> 100 MeV), 3C 279 has been observed to be time variable on the order of a day (Fichtel 1993). The energy output per logarithmic energy interval observed by the Energetic Gamma Ray Experiment Telescope (EGRET) aboard the Compton Gamma Ray Observatory (GRO) in the high-energy γ -ray band above 100 MeV is larger than in any other frequency band (Hartman et al. 1992). The spectrum of the detected emission is well represented by a power law ($kE^{-\alpha}$) of photon spectral index $\alpha = 2.02 \pm 0.07$. If the emission from 3C 279 is isotropic, its γ -ray luminosity between 100 MeV and 10 GeV is about $L_\gamma \simeq 1.6 \times 10^{51}$ photons s $^{-1}$, or $\simeq 1.1 \times 10^{48}$ erg s $^{-1}$, for $H_0 = 75$ km s $^{-1}$ Mpc $^{-1}$. However, it may very well be that this emission is beamed; then for 1 steradian, the true luminosity would be $L_\gamma \sim 9 \times 10^{46}$ erg s $^{-1}$. For comparison, our own Galaxy emits $\sim 5 \times 10^{38}$ erg s $^{-1}$. The overall characteristics of the observed spectrum in the γ -ray regime suggest the presence of an extraordinary source of relativistic particles with an energy spectrum at least as hard as that observed for charged cosmic rays near Earth. There is no way of knowing from the GRO data

whether this spectrum extends across the many additional decades to the extreme energy required by the extragalactic part of the cosmic ray spectrum. Many of the 20 AGNs detected by EGRET appear to have flat spectra and might be expected to be detected at TeV energies (Weekes 1993).

3.3. 3C 273

Quasar 3C 273 (Fig. 1b) is radio loud; unlike 3C 279, it is not an OVV quasar. It has a redshift $z = 0.158$, implying a distance $d \simeq 6.3 \times 10^2$ Mpc ($H_0 = 75 \text{ km s}^{-1} \text{ Mpc}^{-1}$). At X-ray ($2 - 10$ keV), with $H_0 = 50 \text{ km s}^{-1} \text{ Mpc}^{-1}$, 3C 273 has luminosity of $\sim 10^{46} \text{ erg s}^{-1}$ (Bassani et al. 1985). In the $2 - 60$ keV range, the data is well represented by a power law spectrum having a photon index of $\alpha = 1.4 \pm 0.02$. At X-ray ($20 - 200$ keV), $L_x \sim 5 \times 10^{46} \text{ erg s}^{-1}$, a very hard spectrum ($\alpha = 1.2$), with no apparent break or cut-off up to around 200 keV. The soft X-ray is well known for large factor flux variations on timescales \sim hours to days. At hard X-ray energies, observations show the luminosity increasing by a factor of 3 on a timescale of 2 years. At γ -ray ($50 - 800$ MeV), $L_\gamma \sim 4 \times 10^{46} \text{ erg s}^{-1}$. The GRO observations done by EGRET (1991) show a small variation in the flux density from that of the COS-B observations (1976-1980) in the energy range $\sim 50 - 800$ MeV (compare Fig. 1b). The COMPTEL (1991) aboard the GRO measured a photon spectral index $\alpha \simeq 2.3$ for energies between $\sim 10 - 30$ MeV (Hermesen et al. 1993). EGRET (1991) observations of 3C 273 (von Montigny et al. 1993) measured $\alpha \simeq 2.4$ for energies between $\sim 100 \text{ MeV} - 3 \text{ GeV}$.

4. SCENARIO TO EXPLAIN THE ENERGY SOURCE

4.1. ADAFs and Two-Temperature Bistable Accretion Disk Models

It is assumed that the accretion disk surrounding the KBH is the two-temperature, bistable disk model [also referred to as the thin disk/ion corona, and recently, the corona phase called an advection dominated accretion flow (ADAF)]. Such an accretion disk can possibly exist in either phase, thin disk or ion torus, or both (thin disk/ion corona)—while oscillating between the two (Chen & Taam 1996; Narayan 1997; see also Esin, McClintock, & Narayan 1997 and references therein). The two-temperature disk model was first proposed by Shapiro, Lightman and Eardley (1976) to account for the *high* and *low* states of the Galactic X-ray source Cygnus X-1. In the standard thin disk model (Shakura & Sunyaev 1973; Novikov & Thorne 1973), it is assumed that the gas at each radius is in a nearly Keplerian orbit. Slow radial infall occurs as viscosity [including magnetic (Eardley & Lightman 1975; Balbus & Hawley 1991)] transfers angular momentum outward; that is, the gas must give up some of its angular momentum before it can cross the event horizon. The binding energy released by accretion may then be retained by the gas of the disk in the form of heat or radiated away. An accretion flow which is able to radiate away most of its binding energy forms a thin accretion disk; the alternative form is a geometrical thick disk or an ion corona—sometimes referred to as a hot torus (Rees et al. 1982). The possible

formation of a thick disk was first realized through Lightman’s (1974a, 1974b) investigation of the instability of a thin, time-dependent accretion disk around a black hole. His calculations show that as time progresses, density and thermal instabilities develop in the thin disk, causing the material to clump into high-density zones and low-density zones—that become optically thin, bringing about extremely high temperatures, which cause the vertical height h of the inner region to rise quickly. However, without a satisfactory relativistic time-dependent model to treat $h > r$, we can only speculate about properties of the disk as h becomes relatively large. Among these speculations are the following: (1) The rapidly rising internal temperatures could cause the temperature gradient to become superadiabatic, and thus, drive convective (Lightman 1974a; Narayan & Yi 1994) or advective (Abramowicz et al. 1988; Abramowicz et al. 1996) energy transport at a rate necessary to counterbalance the energy released, and an ion corona/hot torus (or ADAF) forms in the inner radii. (2) The rings probably destroy themselves by explosion or supersonic turbulence (Thorne & Price 1975), causing the density in the optically thin regions to once again rise, making cooling processes more efficient; and after this, the disk will most likely settle back down to its thin disk structure, subsequently repeating the instability cycle. Note, the above mentioned density and thermal instabilities are commonly referred to as the “Lightman instabilities.” Such stability and instability phases of the accretion disk, proposed in the items above, can generally be explained in the context of the accretion rate \dot{M} versus surface density Σ plane (Abramowicz et al. 1988; Abramowicz et al. 1995).

Thin disks are primarily thermal emitters, with spectra peaking in the UV; however, the inner region of a thin disk is capable of producing both an UV thermal component and a power law continuum, if surrounded by a corona (hence, the thin disk/ion corona model), since the corona can be heated to temperatures $> 3 \times 10^9$ K by the Lightman instabilities. A detailed model of the thin disk (without the Lightman instabilities) surrounding a KBH gives a surface temperature in the range of $\sim 4 \times 10^6$ K (0.4 keV) to 4×10^7 K (3.5 keV) for the inner region (Novikov & Thorne 1973). But once the instabilities set in, the ionized corona can have electron and proton temperatures as high as $\sim 10^9$ K and $\sim 10^{12}$ K, respectively (Shapiro, Lightman, & Eardley 1976). Because of the high electron and ion (or proton) temperatures attainable in the corona, the basic output radiation is mostly nonthermal γ -rays. The ion corona is a poor radiator; and if the binding energy released is small, funnels can form about the polar axes, which could enable collimation and the formation of jets (Rees et al. 1982). In addition, it has been found independently by Williams (1991, Paper 1), and de Felice and Calvani (1972); de Felice and Curir (1992), that the KBH naturally gives rise to vortical escaping orbits, which are collimated about the polar axis; for example, the Penrose scattered particles discussed here, as we shall see in § 4, exhibit such collimation. From these findings, and a subsequent detailed analysis (de Felice & Carlotto 1997), one can safely say that the KBH is most likely responsible for the initial collimation of the jets.

Before proceeding, I want to pause briefly to explain the origin of this collimation. The physical mechanism responsible for the collimation is the inertial frame dragging, sometimes referred to as the Lense-Thirring effect: due to the gravitational force associated with a rotating mass—it is a

purely general relativistic effect. This component of the gravitational force is sometimes called the “gravitomagnetic” force (Thorne, Price, & Macdonald 1986); it is the the gravitational analog of a magnetic field, which distorts spacetime and acts on the space momentum vector of a test particle in its field. The Lense-Thirring effect or the frame dragging is an intrinsic part of the Penrose mechanism. Inside the ergosphere, where Penrose processes operate, as matter is made to rotate in the direction of the KBH, it acquires large angular momentum and energy from the black hole. The particles inside the ergosphere that have nonequatorially confined orbits will have in addition nonzero polar coordinate momenta (Wilkins 1972; Paper 1; Williams 2002a, 2001). If these highly blueshifted particles were allowed to escape, they would escape along vortical trajectories, as point out by de Felice & Carlotto (1997), i.e., due to the inertial spacetime frame dragging of their orbits. These authors define such trajectories as gravitational spacetime “geometry-induced collimation.” Generally, in these Penrose processes, the incident particles, after scattering in the ergosphere, take with them the energy and momentum of the orbiting targets. This, along with the gravitomagnetic force, enables the escaping Penrose scattered particles to leave the KBH in the form of vortically orbiting relativistic particles, collimated about the polar axis (Williams 2002a, 2001). In summary, the collimation is the characteristic structure of geodesic orbits escaping from the ergosphere or region close to the event horizon of a KBH: this is due to the Lense-Thirring effect, and, hence, is seen here in the four-momenta of these Penrose scattered escaping particles.

Now continuing, on Table 1, model parameters are given for the inner region of a thin disk/ion corona two-temperature, bistable, fully relativistic accretion flow surrounding a KBH ($M = 10^8 M_\odot$, $a/M = 0.998$). These model parameters have been calculated from several sources (Novikov & Thorne 1973; Eardley & Lightman 1975; Eilek 1980; Eilek & Kafatos 1983). Note, Eardley & Lightman (1975) provide the conditions for instability to set in, i.e., in going from a thin disk to ADAF (see Appendix C of that paper). The parameters are defined as follows: α is the viscosity parameter ($0 < \alpha \leq 1$); $y \equiv (4kT_e/m_e c^2) \max(\tau_{\text{es}}, \tau_{\text{es}}^2)$ is the dimensionless parameter that characterizes Comptonization, commonly called the Kompaneets parameter; \dot{M} is the sub-Eddington accretion rate; T and T_s are the thermal and surface temperatures, respectively; T_e and T_i are the electron and ion temperatures, respectively; r_{inner} and $r_{\text{instability}}$ give approximate values for the extent of the inner region and the hot optically thin region of instability, respectively; L_{bol} is the bolometric luminosity; L_γ is the luminosity of the π^0 -induced γ -rays in the ADAF; and h is the height of the disk. The radius at which these values are calculated is $r = 1.3M \approx r_{\text{ms}}$ [model implied inner edge of the dynamically stable thin disk: with a soft X-ray inner region, i.e., where the calculated relativistic correction function $Q(r) \rightarrow 0$ (Novikov & Thorne 1973; Page & Thorne 1974)¹]. Note, unsaturated Comptonization gives $y \sim 1$ and is appropriate whenever there is a copious source of soft photons in the inner hot region (Shapiro & Lightman 1976), whereas saturated Comptonization characterized by $y \gg 1$ is appropriate in the inner region of the cool disk model (Shakura & Sunyaev 1973). The input parameters are α , y , \dot{M} , M , r , and β . All other

¹The behavior of $Q(r)$ in the inner region between the limits $1.2 \lesssim r/M \lesssim 1.28$ needs further investigation: for it is not clear why $Q(r) \rightarrow 0$ at the end points and is < 0 within the limits, irrespective of M .

values are calculated from the references cited above. The extent of the inner and optically thin regions depend on a , α , M , and \dot{M} . Specifically, the regions r_{inner} and $r_{\text{instability}}$ are calculated from Eardley and Lightman (1975). Moreover, notice the following: (1) Increasing α , the viscosity parameter, as in model cases 3 and 6, decreases T , T_e , T_i , and increases T_s , L_γ , and the extents of the regions r_{inner} and $r_{\text{instability}}$. (2) The bolometric luminosity L_{bol} increases with increasing β , M , or \dot{M} —unstable accretion flows could cause β to vary. (3) In all cases, the height of the disk h after instability sets in is less than r_s , where r_s is the assumed radius at which the scattering takes place.

The numerical disk model of Table 1 gives values inward to the photon orbit r_{ph} ($\simeq 1.074M$) for the region of instability. However, the gravitational physics of the rotating KBH will set the minimum radii for the location of the disk particles. Normally, for a steady-state accretion disk surrounding a canonical KBH, the plasma moves in slowly in Keplerian fashion, until it reaches r_{ms} . The inner region of the disk ends here and material particles quickly free-falls into the black hole; hence, the density of matter builds to a maximum at r_{ms} and then falls quickly to zero inside this radius (Novikov & Thorne 1973; Leiter & Kafatos 1978); r_{ms} is sometimes referred to as the last stable orbit. Now, if Lightman instabilities develop in the disk, large amounts of plasma may attain temporary Keplerian orbits within the region between r_{ms} and r_{mb} for material particles, and inward to r_{ph} for massless particles. Such disk particles could very well populate the orbits of the target particles participating in the Penrose scattering processes (described in details in Paper 1, and summarized in the following sections). On Table 1, I have set the minimum inward radius for the region of instability equal to r_{mb} ; however, trapped photons will be able to exist beyond this radius, to r_{ph} , without falling quickly into the event horizon.

4.2. Penrose Scattering Processes

Now summarizing the astrophysical results of Paper 1, Monte Carlo computer simulations of Compton scattering and e^-e^+ pair production ($\gamma\gamma \rightarrow e^-e^+$) in the ergosphere of a KBH are presented: Specifically, I calculate the energy-momentum four-vectors of the resulting Penrose scattered particles. Particles compatible with a thin disk/ion corona accretion surrounding the black hole are assumed to infall along radial geodesics in the equatorial plane inside the ergosphere and scatter off tangential target particles that are in bound orbits. These orbits consist of equatorially confined ($Q = 0$; see eq. [4]) and nonequatorially confined ($Q > 0$) orbits. The equations that govern the orbital trajectory of a particle about a KBH are solved (Paper 1) to determine analytic expressions for the conserved energy E and azimuthal angular momentum L of material and massless particles that have orbits not confined to the equatorial plane. The escape conditions to determine whether or not a particle escapes from the potential well of the KBH are applied to the scattered particles. As stated previously, the Penrose mechanism in general allows rotational energy of the KBH to be extracted by scattered particles escaping from the ergosphere to large distances from the black hole (or to infinity). The results of these model calculations, as we shall see

in more details below, show that the Penrose mechanism is capable of producing the observed high energy particles emitted by quasars and other AGNs. This mechanism, as applied in the model of Paper 1, can extract hard X-ray/ γ -ray photons from Penrose Compton scatterings of initially low energy UV/soft X-ray photons by target orbiting electrons inside the ergosphere (discussed further in § 4.2.1). These model calculations also allow relativistic e^-e^+ pairs to escape, after being produced by infalling low energy photons interacting with highly blueshifted energetic target photons (in bound nonequatorially confined orbits) at the photon orbit: This PPP ($\gamma\gamma \rightarrow e^-e^+$) process may be the origin of the ultrarelativistic electrons inferred from observations to emerge from the cores of AGNs (discussed further in § 4.2.2).

4.2.1. Penrose Compton Scattering

In the PCS processes investigated, photons are assumed to be emitted from material that has fallen inward from infinity and scatter off tangentially equatorially (or nonequatorially) confined orbiting electron rings of completely ionized plasma, revolving near the event horizon, between the marginally stable ($r_{\text{ms}} \simeq 1.2M$) and the marginally bound ($r_{\text{mb}} \simeq 1.089M$) circular orbits. The bound unstable orbits are chosen for the target particles because such orbits can be made, if perturbed slightly, to spiral inward or escape outward, thus increasing the efficiency of the Penrose mechanism. For simplicity, the conditions that the infalling photon encounters in its free fall through the ergosphere before arriving at the designated scattering radius are ignored in these calculations. Otherwise, conditions such as the particle density in the ergosphere and radiative transfer effects would have to be incorporated into the calculations along the null geodesic of the photon. It is assumed that these conditions cause little qualitative change in the results. This assumption has been to some extent validated in the Penrose analysis by Piran and Shaham (1977b), and was used also by these authors in their analysis (Piran & Shaham 1977a, 1977b).

Now, some of the photons, after being scattered by the electrons, escape to infinity. An observer at infinity, observes a low-energy (in most cases $< \mu_e = 0.511$ MeV) photon being scattered by a direct orbiting electron, after which the photon comes out with a higher energy (inverse Compton scattering). Subsequently, the target electron may recoil to another direct orbit of lesser energy (defined as a *quasi*-Penrose process), or the electron may be put on a retrograde orbit of negative energy (a classical Penrose process); in both cases, the target electron gives up energy as measured by an observer at infinity. However, to a particular local frame observer this is just a normal Compton scattering process in which the photon loses energy to the electron, since the photon arrives at the local frame with initial energy higher than $\sim \mu_e$.

Putting the PCS results (discussed in details in Paper 1) into an astrophysical context, it is concluded that this process may play an important role in the upgrading of UV photons ~ 5 eV, say from a thin disk/ion corona accretion, to X-ray photons $\sim 15 - 218$ keV; and in upgrading soft X-ray/hard X-ray photons $\sim 0.511 - 150$ keV, also from a thin disk/ion corona accretion, to hard X-ray/ γ -ray photons ~ 53 keV–12 MeV: contributing to the high energy observed spectra

of AGNs. In addition, because many of the escaping γ -rays have negative radial momenta (out from the $\Theta = 90^\circ$ plane) and nonzero polar and azimuthal coordinate angular momenta, these γ -rays could possibly aid, along with magnetic fields and relativistic electrons, in the formation of the observed astrophysical jets commonly seen in AGNs (see Williams 2002a). Such vortical-like escaping orbits which are naturally collimated about the axis of symmetry (the rotation axis) due to the spin of the KBH have been described by de Felice and Curir (1992) and de Felice and Carlotto (1997). Their description gives support to the Penrose theoretical model calculations presented in this present paper. A detailed discussion of these vortical orbits produced in Penrose processes is given by Williams (2002b; see also 2001).

Features of the PCS photons are shown in the energy-momentum spectra of Figures 2 and 3. The radial and azimuthal momentum components are plotted in Figures 2a and 2b for a typical PCS of 2000 incoming photons. Depicted in Figure 3 are polar momentum components for two PCS cases. Compare Figures 3a and 3b; notice the asymmetry in the polar directions: the one-sided distribution favors the positive Θ -direction. This feature could be extremely important in jet formation (Paper 1). Such asymmetry in the distribution of the scattered particles is a general relativistic effect, due to the gravitomagnetic (GM) field, which causes the extreme dragging of inertial frames in the ergosphere of a rotating black hole, and exerts a force on the momentum vector of a particle in its field (Williams 2002a, 1999), as mentioned earlier. Williams (2002a) presents a detailed investigation of the gravitomagnetic field and Penrose processes, showing that the GM field alters incident and outgoing angles of the Penrose scattered particles, appearing to break the reflection symmetry of the Kerr metric above and below the equatorial plane. This asymmetry, due to the GM field, has recently been confirmed by an independent analysis (Bini et al. 2002).

The corresponding polar angles of the escaping particles, above and below the equatorial plane ($\Theta = 90^\circ$), as measured by an observer at infinity, for the cases in Figure 3, are displayed in Figure 4. These polar angles are derived from equation (4) by letting $P_\Theta \rightarrow 0$ (see also Piran & Shaham 1977a); thus, in general,

$$\delta = \arccos \left[\frac{-T + \sqrt{T^2 - 4SU}}{2S} \right]^{1/2}, \quad (6)$$

where

$$\begin{aligned} S &\equiv a^2(\mu_o^2 - E^2); \\ T &\equiv Q + a^2(E^2 - \mu_o^2) + L^2; \\ U &\equiv -L^2 \end{aligned}$$

(δ is measured relative to the equatorial plane).

Figures 2a, 3 and 4 show that the KBH scatters most of the photons into the polar direction, at an angle $\Theta'_{\text{ph}} (= 90^\circ \mp \delta_{\text{ph}}$, for escaping above “−” or below “+” the equatorial plane, where

$\delta = \delta_{\text{ph}}$ is given by eq. [6]), and naturally produces one-sided jets of particles; see Williams (2002a) for details. Moreover, the particles that are scattered with nonzero azimuthal and nonzero polar coordinate momentum components (compare Figs. 2b and 3b) give rise to vortical orbits concentric about the polar axis, with corresponding polar angles of escape (Fig. 4b) indicating a coil-like collimation (Williams 2002b, 2001). Note that, photons escaping with the highest energy, after being scattered by the nonequatorially confined orbiting target electrons, have polar angles of escape approximately equal to that of the maximum latitudinal angle—relative to the equatorial plane—of the target electrons ($\delta \sim 30^\circ$; compare Fig. 4b, and see § 4.4 for further explanation of the latitudinal angle). Similarly, the highest energy PCS photons by equatorially confined target electrons have δ_{ph} values near the equatorial plane (compare Fig. 4a).

The calculated luminosity spectra resulting from the above described PCS processes are presented in § 5, where they are compared with observations.

4.2.2. *Gamma Ray-Gamma Ray Penrose Pair Production (PPP)*

This PPP ($\gamma\gamma \longrightarrow e^-e^+$) consists of collisions inside the ergosphere, between radially infalling photons and bound circularly orbiting photons, at the radius of the photon orbit (Bardeen et al. 1972):

$$r_{\text{ph}} = 2M\{1 + \cos[(2/3)\arccos(-a/M)]\}, \quad (7)$$

where r_{ph} represents an unstable circular orbit. This orbit is the innermost boundary of circular orbits for particles i.e., for massless particles (the marginally bound orbit r_{mb} is the innermost orbit for material particles). The initial energies used in these calculations, as measured by an observer at infinity, for the infalling photon and the orbiting photon, $E_{\gamma 1}$ and $E_{\gamma 2}$, respectively, are in the following ranges: $3.5 \text{ keV} \leq E_{\gamma 1} \leq 1 \text{ MeV}$ and $3.4 \text{ MeV} \lesssim E_{\gamma 2} \lesssim 3.89 \text{ GeV}$ [defined by eqs. (A20) and (A21) of Paper 1 for given Q values]. These ranges are consistent with those produced by thin disk/ion corona models. The high energy range for $E_{\gamma 2}$ is chosen based on the expected blueshift in the energy of a photon at the photon orbit (recall from § 1 that the blueshift factor at the photon orbit for a KBH with $a = 0.998M$ is $\simeq 52$). The γ -rays produced in Eilek’s hot accretion disk model (Eilek 1980; Eilek & Kafatos 1983), with energies up to $\sim 100 \text{ MeV}$, can very well be seed photons (now blueshifted and bound at the photon orbit) for these PPP ($\gamma\gamma \longrightarrow e^-e^+$) processes (Eilek 1991). In addition, some of the PCS photons, described in the last section, can also be seed particles for these processes (Paper 1). The target photons having orbital energies, $E_{\gamma 2}$, within the range given above, have corresponding Q values within the range of $0.099 Mm_e \leq \sqrt{Q_{\gamma 2}} \leq 113 Mm_e$, and their maximum latitudinal orbiting angles (relative to the equatorial plane) are $\approx 0.5^\circ$, as given by equation (6), irrespective of their individual values of $E_{\gamma 2}$, $L_{\gamma 2}$, and $Q_{\gamma 2}$.

The results of these PPP ($\gamma\gamma \longrightarrow e^-e^+$) processes (Paper 1), and the calculated luminosity presented in § 5, show that this can be an important way, if not the dominant way, to extract the extremely relativistic e^-e^+ pairs that are inferred from observations to be emerging from the cores

of AGNs.

Note that, these PPP ($\gamma\gamma \longrightarrow e^-e^+$) processes are classified as quasi-Penrose processes (Paper 1). That is, the target particle is not specifically put on a negative energy orbit as in the classical Penrose extraction of rotational energy, yet rotational energy is still extracted, however, indirectly, from the highly energetic photons, that have been blueshifted by the KBH, at (or near) the photon orbit; see Paper 1 for further details.

In general, a possible picture of what takes place in these PPP ($\gamma\gamma \longrightarrow e^-e^+$) processes to an observer at infinity (i.e., the BLF) is the following: low energy unbound infalling photons interact with high energy bound photons at the photon orbit producing pairs of relativistic electrons with energies as high as ~ 4 GeV or higher—depending on the type of accretion flow; about 50% of these produced e^-e^+ pairs escape from the potential well of the KBH. Typical radial and azimuthal energy-momentum spectra of the e^-e^+ pairs are shown in Figure 5. These copiously produced relativistic escaping electrons can participate in astrophysical processes intrinsic to observations of AGNs, such as the production of the synchrotron radiation and the formation of the jets. Notice in Figure 5a that only the positive radially directed e^-e^+ pairs escape; this is to be expected since all negatively directed material particles at radii less than r_{mb} must fall directly into the KBH. Also, it is important to note here that if these PPP ($\gamma\gamma \longrightarrow e^-e^+$) processes had not occurred, photons in the photon orbit would, most likely, not have had any other way of escaping, and the energy released in these processes would have been forever trapped by the KBH. The reason for this is given by Bardeen et al. (1972). It is pointed out that, in order for a photon to escape from the circular photon orbit, since nothing can come out of the hole, some physical process near the hole is necessary to inject a particle into an escaping trajectory, i.e., from a plunging orbit into an escaping one.

Depicted in Figure 6 are polar coordinate momentum components for various PPP ($\gamma\gamma \longrightarrow e^-e^+$) cases; the corresponding angles of escape, of the e^-e^+ pairs, above and below the equatorial plane, as given by equation (6), are shown in Figure 7. Notice in Figures 6 and 7, the increase in the asymmetry of the e^-e^+ pair distributions as the escaping energies increase; this is consistent with the effects caused by the GM field (Williams 2002a). Moreover, such one-sidedness could be an important factor in explaining the asymmetry in the observed jets of AGNs. Thus, as in the PCS case, we find that the KBH in these PPP ($\gamma\gamma \longrightarrow e^-e^+$) processes naturally produces uneven fluxes of relativistic particles above and below the equatorial plane. In addition, also as in the PCS, we find that the e^-e^+ pairs escape along vortical orbits concentric about the polar axis, and highest energy pairs escape with polar helical angle $\delta = \delta_{\mp} \sim 0.5^\circ$ (eq. [6]); this suggests strong coil-like jet collimation (Williams 2002b, 2001). Note that, this angle of escape for the highest energy e^-e^+ pairs is approximately equal to that of the maximum latitudinal angle—relative to the equatorial plane—of the target nonequatorially confined orbiting photons (compare Figure 7; and see § 4.4 for further explanation of the latitudinal angle).

The above findings are consistent with observations of AGNs. In the following sections, I shall

discuss further this PPP ($\gamma\gamma \rightarrow e^-e^+$) and its probable role in astrophysical black hole sources.

4.3. Penrose Processes and the Classical Thin Disk

In the PCS and PPP ($\gamma\gamma \rightarrow e^-e^+$) processes considered in this paper, the lowest energies (0.511 keV–3.5 keV) used for the infalling photons are consistent with the surface temperature ($T_s \simeq 4 \times 10^6 \text{ K} - 4 \times 10^7 \text{ K}$, at $r \approx 1.3M$, for $M = 10^8 M_\odot$) of the classical thin disk accretion model about a KBH (Novikov & Thorne 1973). Now, the scenario for a $10^8 M_\odot$ KBH, surrounded by a classical thin disk (i.e., before the Lightman instabilities set in) is the following. About 80% of the initially infalling soft X-rays ($\sim 3.5 \text{ keV}$), that have undergone PCS by equatorially confined orbiting target electrons (at $\sim r_{\text{mb}}$, $E_e \sim 0.54 \text{ MeV}$), can escape with boosted energies as high as hard X-rays ($\sim 0.26 \text{ MeV}$), while the others either fall into the KBH, or become bound (i.e., with a turning point) at the photon orbit—acquiring blueshifted energies as high as $\sim 14 \text{ MeV}$. The polar coordinate momentum components $(P'_{\text{ph}})_\Theta$ of the scattered photons reveal that indeed such PCS photons can acquire the necessary Q values to populate the photon orbit by the criteria discussed in Paper 1 [i.e., the Q value must match that of the photon orbit whose energy is consistent with the expected blueshifted energy, within reason, as defined by equation (2.26) of Paper 1; see also discussion in Williams (2002a)]. These blueshifted photons, now assuming to have populated the photon orbit, can undergo PPP ($\gamma\gamma \rightarrow e^-e^+$) processes with infalling soft X-rays [for maximum absolute efficiency (Paper 1)], producing e^-e^+ pairs with energies as high as $\sim 13 \text{ MeV}$. About half of the produced pairs escape along vortical helical-like orbits collimated about the polar axis. The helical angle of escape δ_{esc} , defined relative to the equatorial plane (see equation [6] and Fig. 7a), is $\sim 5^\circ$ down to $\sim 0.5^\circ$ for the highest energy particles, implying strong coil-like collimation (Williams 2001, 2002b). Thus, I conclude, that, due to PCS and PPP ($\gamma\gamma \rightarrow e^-e^+$) processes, in a classical thin disk, the highest particle energies attainable for the PCS photons are $\sim 260 \text{ keV}$ (hard X-rays); and for the relativistic PPP ($\gamma\gamma \rightarrow e^-e^+$) electrons, the highest energies attainable are $\sim 13 \text{ MeV}$. Yet, without these Penrose processes, as can be seen above from the surface temperature T_s , the highest energy radiated by a classical thin disk surrounding a supermassive KBH is $\sim 3.5 \text{ keV}$, and, of course, no pair production (compare Table 1).

4.4. Penrose Processes and the Thin Disk/Ion Corona

Since the disk can exist between two phases [thin disk/ion corona (or hot torus)] the occurrence of the Lightman instabilities can act to enhance the Penrose process, thereby contributing to observed variabilities and particle energies up to $\sim \text{GeV}$. We shall see this in the following scenario for a $10^8 M_\odot$ KBH surrounded by a thin disk/ion corona. In this scenario, X-rays ($\sim 0.03 - 0.15 \text{ MeV}$), after undergoing PCS by equatorially confined orbiting target electrons, can escape with boosted energies ranging from $\sim 0.7 \text{ MeV}$ up to $\sim 2 \text{ MeV}$. Just as in the classical thin disk, about 80% of the PCS photons can escape, while the others either fall into the KBH, or

become bound at the photon orbit upon acquiring blueshifted energies, however, in these cases, the energies acquired range from ~ 36 MeV to as high as ~ 104 MeV. The polar coordinate momentum components of such PCS photons reveal that indeed they can acquire the necessary Q values to populate the photon orbit in the above blueshifted energy range (Paper 1). Subsequently, the blueshifted photons, now assuming to have populated the photon orbit, can undergo PPP ($\gamma\gamma \rightarrow e^-e^+$) processes with infalling disk soft X-rays, producing e^-e^+ pairs that can escape with energies as high as ~ 100 MeV.

Now we assume that the photon orbit can be populated in addition by γ -rays from the π^0 decays ($\pi^0 \rightarrow \gamma\gamma$), occurring in Eilek’s (1980) ion corona/hot torus model (discussed in §§ 1, 4.2, and Paper 1). These γ -rays are created with energies narrowly peaked around $E_\gamma \simeq 75$ MeV. Such γ -rays can be blueshifted to energies ~ 4 GeV, as they become populated or bound at the photon orbit. Subsequently, infalling soft X-rays from the disk can undergo PPP ($\gamma\gamma \rightarrow e^-e^+$) with these now bound γ -rays, producing e^-e^+ pairs that can escape with energies up to ~ 4 GeV. Recently, it has been shown that if the proton distribution in Eilek’s hot torus model (or ADAF) is a power law, the energy of the γ -rays, produced by the π^0 decays, can reach energies > 100 MeV (Mahadevan, Narayan, & Krolik 1997). Therefore, since the blueshift is $\simeq 52$ at the photon orbit, the PPP ($\gamma\gamma \rightarrow e^-e^+$) can produce e^-e^+ pairs with energies > 5 GeV. However, here in this present analysis only the γ -ray particles from Eilek’s model, with energies $\lesssim 100$ MeV, before becoming blueshifted, need to be considered. Such infalling particles allow these Penrose processes to explain the γ -ray spectra of 3C 279 and 3C 273. Note, assuming that Eilek’s particles (or particles from ADAFs) will acquire the necessary Q value appears to be a valid assumption, based on the fact that the PCS photons acquire the necessary Q value to populate the photon orbit. That is, one would expect the proton-proton nuclear reaction π^0 emission (Eilek & Kafatos 1983; Mahadevan et al. 1997), and the subsequent π^0 decay: $\pi^0 \rightarrow \gamma\gamma$, to be Penrose processes, and thus, the π^0 -induced γ -rays are expected to acquire the appropriate Q values. However, confirmation of this will have to await a Penrose process analysis of these reactions in the ergosphere of a KBH (Williams & Eilek 2002).

Moreover, if we assume that pairs produced in Eilek’s hot torus model, which have energies peaked around $\simeq 35$ MeV, can populate the nonequatorially confined target electron orbits, say in the range of $\sim 6 - 12$ MeV, then PCS of infalling soft X-ray/UV photons from the disk allows most of the scattered photons to escape with boosted energies up to ~ 12 MeV: this value is consistent with one of the general cutoffs observed in the spectra of quasars (compare Fig. 1). Note that, such target electrons have nonequatorially confined ($Q > 0$) “spherical-like” orbits (Wilkins 1972), and reach latitudinal angles in their orbits $\lesssim 30^\circ$, above and below the equatorial plane, as given by equation (6). The relevant algebra to determine the conserved energy E and azimuthal angular momentum L for these nonequatorially confined spherical-like orbits, for massless and material test particles, can be found in Paper 1 (see also Williams 2002a). One of these spherical-like orbits consists of a particle repeatedly passing through the equatorial plane while tracing out a helical belt lying on a sphere at constant radius. The belt width or the maximum and minimum latitudes

that the particle achieves, in general, increase with increasing Q (this does not appear to be true for massless particles bound at the photon orbit; see § 4.2.2). Now, these PCS γ -rays up to ~ 12 MeV could contribute to the observed spectra in this energy range (as will be shown in § 5). The importance of these PCS γ -rays is that they can acquire and escape with large polar and azimuthal coordinate momenta (implicating collimation), thus supporting the jet formation process (compare Figs. 2, 3*b* and 4*b*). Recently, it has been shown that these nonequatorially confined target electron orbits can be populated by prior PPP ($\gamma\gamma \rightarrow e^-e^+$), up to ~ 2.5 MeV (Williams 2003).

These energies of the escaping Penrose scattered particles are to be compared with maximum energies attainable for the popular two-temperature accretion disk models (Shapiro, Lightman, & Eardley 1976; Lightman & Eardley 1974), such as thin disk/ion corona (ADAF). In these disk models, without Penrose processes occurring, the maximum particle energies attainable are ~ 100 MeV for a thermal distribution of protons (Eilek 1980), and up to ~ 31 GeV for a power law distribution of protons (Mahadevan, Narayan, & Krolik 1997). However, when the Penrose processes PCS and PPP ($\gamma\gamma \rightarrow e^-e^+$) are included, particles can possibly escape with energies as high as ~ 4 GeV up to ~ 54 GeV (attempting to go beyond this value causes the computer code to breakdown, suggesting that the model is attempting to go beyond what is physically possible). In addition, since the luminosity of the escaping π^0 -induced γ rays is so low for ADAFs, due to the bulk of energy being advected radially into the hole, rather than being radiated away, Penrose processes appear needed in order for the high energy particles to escape in the form of jets (i.e., with the Penrose scattered particles being collimated about the polar axis naturally by the KBH). Such particles, as have been found in these calculations, were proposed to exist in de Felice and Curir’s (1992) analysis of the Kerr geometry. The Penrose model calculations presented here and elsewhere (Williams 1991, Paper 1, 2002a, 1999) appear to strongly validate their analysis, as well as the analysis by Bini et al. (2002): concerning the asymmetry in the spherical-like (or nonequatorially confined) particle orbits (Wilkins 1972), above and below the equatorial plane, due to the GM field. Further analysis of the first order perturbation in latitudinal angles Θ_{\min} , Θ_{\max} (Bini et al. 2002) should reveal that the asymmetry is directly related to the first order perturbation in the constant radius r of the spherical-like orbit [see eq. (47) of Williams (2002a)], and, thus, overall related to the hard evidence that the GM field breaks the expected reflection equatorial planar symmetry of the Kerr metric (Williams 1999)².

²Figures 1(c) and 1(d) of Williams (1999) are incorrect. Figures 4(e) and 4(h), respectively, of Williams (2002a) are the correct figures, where in Figure 4(h) the target electrons have both positive and negative equal absolute value polar coordinate angular momenta.

4.5. Secondary Processes

4.5.1. Inverse Compton Scattering and the PPP Electrons

Relativistic inverse Compton scattering of the PCS photons, or accretion disk photons, by the PPP ($\gamma\gamma \rightarrow e^-e^+$) electrons is an important secondary process, which I refer to as “secondary” Penrose Compton scattering (SPCS). In general, the energy of a Compton scattered photon is given by (Kafatos 1980)

$$E_{\text{Comp}} \sim \gamma_e^2 h\nu, \quad (\text{for } h\nu \lesssim m_e c^2 / \gamma_e); \quad (8)$$

or

$$E_{\text{Comp}} \sim \gamma_e m_e c^2, \quad (\text{for } h\nu \gtrsim m_e c^2 / \gamma_e), \quad (9)$$

where γ_e is the Lorentz factor of the electrons (in this case, $\gamma_e = E_{\mp}/m_e c^2$), and $h\nu$ is the original energy of the photon. It turns out that most of the “secondary” Penrose Compton scattered (SPCS) photons satisfy the relation of equation (9) for relativistic Compton scattering. For example, for PPP ($\gamma\gamma \rightarrow e^-e^+$) electrons with energies ~ 2 MeV, all PCS photon or disk photons with energies as high as ~ 0.26 MeV satisfy equation (9); and for electron pairs with energies ~ 200 MeV, all PCS photons or disk photons with energies above $\sim 10^{-3}$ MeV satisfy equation (9).

In the calculated luminosity spectra of the Penrose processes, presented in § 5, the electrons produced by the PPP ($\gamma\gamma \rightarrow e^-e^+$) are allowed to undergo SPCS with infalling photons from the accretion disk. The acquired numerically (Monte Carlo) calculated energies of the SPCS photons are not much different from the maximum attainable energies given by equation (9). In the SPCS, the numerical calculations are similar to those used for the PCS (Paper 1), except now the PPP ($\gamma\gamma \rightarrow e^-e^+$) electrons are used for the targets.

4.5.2. Relativistic Beaming and the PPP Electrons

An important aspect of the above secondary process is beamed relativistic expansion or commonly called relativistic beaming, i.e., when high energy radiation due to Compton scattering is beamed into the polar directions by means of relativistic electrons emanating from the central source—such as the PPP ($\gamma\gamma \rightarrow e^-e^+$) electrons. Such PPP electrons, which are initially collimated by the KBH, and subsequently, perhaps, accelerated by shocks in the gas motions and electromagnetic fields, can possibly give rise to the observed astrophysical jets. In relativistic beaming models, the bulk motion of the electrons (i.e., of a given blob of electrons) is assumed to move with relativistic speed. Superluminal motion, produced by relativistic beaming, becomes important if the jet makes a small angle up to $\sim 15^\circ$ with the line of sight of the observer. Such motion, in so-called superluminal sources, can display apparent jet velocities greater than the speed of light, and can enhance the observed brightness, energy, and variability of the source.

Some theoretical relations for relativistic beaming from various authors, relevant to these present model calculations, are as follows. The relation between the scattered photon energy

E_{Comp} and the original photon energy $h\nu$ is given by (Dermer et al. 1992)

$$\frac{E_{\text{Comp}}}{h\nu} \simeq \frac{(1 - \cos \theta_s)}{[\Gamma(1 - \beta \cos \theta_s)]^2} \gamma_e^2, \quad (10)$$

where $c\beta = v_{\text{bulk}} \equiv v$ is the bulk or space velocity, $\Gamma = (1 - \beta^2)^{-1/2}$ is the Lorentz factor of the blob, and θ_s is the angle between the velocity vector of the blob and the direction of the observer. Equation (10) is for scattering in the Thomson regime, i.e., for $h\nu \lesssim m_e c^2 / \gamma_e \Gamma$ (Sikora, Begelman, & Rees 1994). The energy of the scattered photon in the Klein-Nishina regime, i.e., for $h\nu \gtrsim m_e c^2 / \gamma_e \Gamma$ is given by (Dermer & Schlickeiser 1993)

$$\frac{E_{\text{Comp}}}{m_e c^2} = \frac{1}{\Gamma(1 - \beta \cos \theta_s)} \gamma_e. \quad (11)$$

Notice that equations (10) and (11) reduce to equations (8) and (9), respectively, when $\Gamma = 1$ and $\theta_s = 90^\circ$, as would be expected.

The apparent velocity of the blob in the jet as measured by an observer at infinity is given by (Blandford, McKee, & Rees 1977)

$$v_{\text{app}} = \frac{v \sin \theta_s}{1 - (v/c) \cos \theta_s}. \quad (12)$$

The observed luminosity L_{obs} relative to the intrinsic luminosity L_{intr} is given by (Maraschi, Ghisellini, & Celotti 1992)

$$L_{\text{obs}} = \delta_*^m L_{\text{intr}}, \quad (13)$$

where $\delta_* = [\Gamma - (\Gamma^2 - 1)^{1/2} \cos \theta_s]^{-1}$ is the usual Doppler factor, and m ($= 3 + \alpha$; $\alpha \equiv$ flux spectral index) is between 3 and 4.

For completion, an estimation of the intrinsic size \bar{R} of the γ -ray emitting region is given by the variability time scale t_{var} :

$$\bar{R} = \delta_* c t_{\text{var}}. \quad (14)$$

For example, for angle $\theta_s \sim 5^\circ$, and a typical model value of $\Gamma = 12$, giving $v_{\text{bulk}} = 0.9965c$, we find that $E_{\text{Comp}} = 11.46 E_{\text{intr}}$, where E_{intr} is the intrinsic photon energy (eq. [9]); $v_{\text{app}} = 11.95c$; $L_{\text{obs}} = 5.1 \times 10^3 L_{\text{intr}}$ for $m = 3.5$ and $\delta_* = 11.46$; note, equations (11) through (13) have been used.

Thus, one can see from the above parameters that relativistic beaming near the observers line of sight is indeed an effective enhancement mechanism. However, the relativistic beaming models must rely on some preliminary mechanism to create and collimate the relativistic electrons about the polar axis of the AGN. According to the model calculations presented in this paper, the Penrose process suggests the perfect preliminary mechanism. This mechanism has been shown (Paper 1) to produce relativistic electrons (γ_e up to at least $\sim 10^4$), with vortical escaping orbits about the polar axis (de Felice and Curir 1992; de Felice and Carlotto 1997; Williams 2002b), that

have asymmetrical distributions above and below the equatorial plane—leading to asymmetrical jets (Williams 2002a). Recall, some specific inconsistencies encountered in attempting to use relativistic beaming models alone to explain the asymmetrical jets, without attributing any to being produced intrinsically by the energy source, are discussed in § 1.

5. COMPARISON WITH OBSERVATIONS AND DISK MODEL CORRELATIONS

5.1. Model Calculated Penrose Spectra

The luminosity spectra due to Penrose processes for the specific cases of quasars 3C 279 and 3C 273 are plotted in Figures 8a and 8b, along with their observed spectra for comparison. The outgoing (escaping) luminosity produced by the Penrose scattered particles is given by

$$\begin{aligned} L_{\nu}^{\text{esc}} &\approx 4\pi d^2 F_{\nu}^{\text{esc}} \text{ (erg/s Hz)} \\ &\approx 4\pi d^2 h \nu^{\text{esc}} f_1 f_2 \cdots f_n (N_{\nu}^{\text{in}} - N_{\nu}^{\text{cap}}) \end{aligned} \quad (15)$$

(the units of L_{ν}^{esc} are in the parenthesis), where d is the cosmological distance of the black hole source; F_{ν}^{esc} is the flux of escaping photons; N_{ν}^{in} and N_{ν}^{cap} are the emittance of incoming and captured photons, respectively; f_n defines the total fraction of the particles that undergoes scattering [$n = 2$ for PCS and $n = 5$ for PPP ($\gamma\gamma \rightarrow e^-e^+$)]. The values of f_1, \dots, f_n , which fit the Penrose calculated luminosities with observations for the specific cases of 3C 279 and 3C 273, are given in Tables 2 through 5. As we shall see, the f_n 's are somewhat free parameters. Note, the labeled points on Figure 8 correspond to the case numbers on Tables 2 through 5.

Specifically, the f_n 's are defined as follows: f_1 is the fraction of incident disk photons, intersecting the scattering radius r_s , coming from the inner radius r_d of the accretion disk of height h :

$$f_1 \approx \frac{r_s^2}{r_d h} (\cos \theta_1 - \cos \theta_2) \quad (16)$$

[compare equation (3)]; f_2 is the fraction scattered, dependent on the cross section—the effective area of the target particle [Klein-Nishina or pair production (see Paper 1)], which implies that the fraction of the incoming photons that actually undergoes PCS or PPP ($\gamma\gamma \rightarrow e^-e^+$) is dependent on the incident energies and angles; f_3 is the fraction of the incident photons from the disk that intersects the scattering radius r_s , traveling from an inner radius of the accretion disk r_d , that are free to undergo SPCS with the PPP ($\gamma\gamma \rightarrow e^-e^+$) electrons (similar to f_1); f_4 is the fraction of the incident photons from the disk that actually undergoes SPCS with the PPP ($\gamma\gamma \rightarrow e^-e^+$) electrons (also dependent on the Klein-Nishina cross section and similar to f_2); f_5 is the fraction of the e^-e^+ pairs that undergoes SPCS (dependent on the expansion rate of the jet). So the values of f_1, \dots, f_5 , that are found to agree with observation, indirectly may tell us something about the particle densities in the ergosphere, at different radii, per frequency interval, e.g., number density n_{ν} ($\text{cm}^{-3} \text{ Hz}^{-1}$), radiation density u_{ν} ($\text{erg/cm}^{-3} \text{ Hz}^{-1}$), and mass density ρ_{ν} ($\text{g cm}^{-3} \text{ Hz}^{-1}$).

The incoming surface flux density of the incident photons from the disk participating in the Penrose scattering processes,

$$F_{\nu}^{\text{in}} = h\nu N_{\nu}^{\text{in}}, \quad (17)$$

is determined from spectral observations of 3C 279 and 3C 273 (see Fig. 1). A power law distribution is assumed for the incoming photons:

$$N_{\nu}^{\text{in}} = K\nu^{-\alpha} \left(\frac{\text{number of photons}}{\text{cm}^2 \text{ s Hz}} \right), \quad (18)$$

where, the photon spectral index:

$$\alpha = -\frac{\log N_{\nu_2} - \log N_{\nu_1}}{\log \nu_2 - \log \nu_1}, \quad (19)$$

and K are determined. The values of α and K determined from observations, and used in these calculations for 3C 279 and 3C 273, are the following:

$$\alpha \simeq 1.48, \text{ for 3C 279; between } \nu_1 = 1.166 \text{ keV, } \nu_2 = 2.93 \text{ keV;}$$

$$\alpha \simeq 1.5 \text{ for 3C 273; between } \nu_1 = 0.511 \text{ keV, } \nu_2 = 25 \text{ keV;}$$

and

$$K \simeq 1.29 \times 10^6 \text{ cm}^{-2} \text{ s}^{-1} \text{ Hz}^{0.48}, \text{ for 3C 279;}$$

$$K \simeq 1.132 \times 10^7 \text{ cm}^{-2} \text{ s}^{-1} \text{ Hz}^{0.5}, \text{ for 3C 273.}$$

So, from observations, the initial photon distribution laws for 3C 279 and 3C 273, used in these calculations, are given by

$$N_{\nu_{\text{in}}}^{\text{in}} = 1.29 \times 10^6 \nu_{\text{in}}^{-1.48} \text{ photons cm}^{-2} \text{ s}^{-1} \text{ Hz}^{-1}; \quad (20)$$

$$N_{\nu_{\text{in}}}^{\text{in}} = 1.132 \times 10^7 \nu_{\text{in}}^{-1.5} \text{ photons cm}^{-2} \text{ s}^{-1} \text{ Hz}^{-1}, \quad (21)$$

respectively. Equations (20) and (21) give the emittance of photons per unit area per unit time per unit frequency—based on spectral observations in the soft X-ray regime. Here we are assuming that emitted energy in this regime is due to the accretion disk.

The photon initial (or incoming) distribution law N_{ν}^{in} of equation (18), as defined by equations (20) and (21), is normalized to 2000 photons, such that, the weighted average of each photon per incoming frequency is given by

$$\langle N_{\nu_{\text{in}}}^{\text{in}} \rangle = \frac{N_{\nu_{\text{in}}}^{\text{in}}}{n_{\text{total}}^{\text{in}}} = \frac{N_{\nu_{\text{in}}}^{\text{in}}}{2000}, \quad (22)$$

which states that, one incoming photon is equivalent to $\langle N_{\nu_{\text{in}}}^{\text{in}} \rangle$, where ν_{in} is the incoming frequency, and $n_{\text{total}}^{\text{in}}$ is the total number of the incoming distribution of photons having the given monochromatic frequency ν_{in} . It is important to note that $\langle N_{\nu_{\text{in}}}^{\text{in}} \rangle$ is invariant with respect to a

specific frequency interval, i.e., a constant, meaning that $\langle N_{\nu_{\text{in}}}^{\text{in}} \rangle$ does not change in going from one frequency to another. The above is a statement of the conservation of photon number in Compton scattering processes (assuming that each incoming photon scatters).

Now, using this conservation law, equation (15) can be written as

$$\begin{aligned} L_{\nu}^{\text{esc}} &\approx 4\pi d^2 h \nu^{\text{esc}} f_1 f_2 \cdots f_n \langle N_{\nu_{\text{in}}}^{\text{in}} \rangle (n_{\nu} - n_{\nu}^{\text{cap}}) \\ &\approx 4\pi d^2 h \nu^{\text{esc}} f_1 f_2 \cdots f_n \langle N_{\nu_{\text{in}}}^{\text{in}} \rangle n_{\nu}^{\text{esc}}, \end{aligned} \quad (23)$$

where n_{ν} is the number of the initial photons ($n_{\text{total}}^{\text{in}} \equiv 2000$) scattered into the final frequency interval $\Delta\nu$, i.e., n_{ν} is the number of final photons emitted into a specific frequency interval $\Delta\nu$, with ν being the average frequency of the interval; n_{ν}^{cap} is the corresponding number of final photons captured by the black hole at the frequency interval $\Delta\nu$; and n_{ν}^{esc} is the number of final photons that escape from the black hole at the frequency interval $\Delta\nu$. Note that, $n_{\nu} = n_{\nu}^{\text{cap}} + n_{\nu}^{\text{esc}}$; and $\sum_{\nu} n_{\nu} = n_{\text{total}}^{\text{in}} = 2000$. In general, to determine the outgoing Penrose luminosity L_{ν}^{esc} , several values of ν_{in} , consistent with observations, are separately used in equation (22); the result of each distribution of 2000 infalling monochromatic photons is then substituted into equation (23), along with Penrose model calculated values of n_{ν}^{esc} at ν^{esc} , and other appropriate model parameters. From this we obtain several distributions of outgoing luminosities over specific frequency ranges. The peak luminosity of each outgoing distribution, at the corresponding ν^{esc} (i.e., the continuum) is then plotted, as discussed in the following section.

5.2. Agreement with Observations of 3C 279 and 3C 273

The model luminosity spectra resulting from equation (23) for the Penrose processes considered here, specifically for quasars 3C 279 and 3C 273, are plotted in Figures 8a and 8b, respectively. The solid lower line curves are the observed spectra in the X-ray, soft γ -ray, and γ -ray regimes.

On Figure 8a, for 3C 279, the crosses located at points 2 through 5 are from PCS at $r_{\text{ms}} = 1.2M$, $r = 1.13M$, $r = 1.1M$, and $r_{\text{mb}} = 1.089M$, respectively, by equatorially confined target electrons. These radii cover the scattering region of the ergosphere one would expect the PCS to occur. In order for the PCS by equatorially confined targets to contribute to the observe spectrum in the X-ray regime, the points 2 through 5 must lie directly above the observed curve—as one can see they do not. Thus, it appears that PCS by equatorially confined target electrons contributes little, if any, to the X-ray part of the spectrum. However, this is true only if we assume, from observations, that the infalling photons undergoing PCS are of the same distribution we observe in the part of the spectrum we believe to be intrinsic to the accretion disk. Now, the general curve for PCS by equatorially confined targets is shown [the dotted line (or curve) between points 1 and 7]. In the general case, lower energy photons (those not observed in the spectrum of 3C 279, but are consistent with the two-temperature, bistable thin disk/ion corona accretion) are used in the PCS by equatorially confined target electrons at r_{mb} . One sees that part of the general PCS curve lies

directly above the observed curve, meaning that it could contribute to the observed spectrum; but in order for this to be possible, the infalling disk photons would have to have energies lower than what is observed for 3C 279. Nevertheless, to produce the general curve, the infalling disk photons have energies between $E_{\text{ph}} = 0.07$ keV ($\log \nu/Hz = 16.23$) and 150 keV ($\log \nu/Hz = 20.56$) to give final energies in the range of $E'_{\text{ph}} \simeq 7.28$ keV ($\log \nu/Hz = 18.25$) and 1.5 MeV ($\log \nu/Hz = 20.56$), respectively. Table 2 gives the values of the factors f_1 and f_2 of equation (23) used in these model calculations. Note, the lack of observed emission in the region attributed to the accretion disk may be due to jet beamed emission near the line of sight (§ 4.5.2), blocking from view emission from the disk.

Further, on Figure 8a, the general PCS spectrum produced by the nonequatorially confined target electrons at r_{mb} , and infalling monochromatic photons with energy $E_{\text{ph}} = 0.03$ MeV, is represented by the dotted curve in the soft γ -ray regime; the nonequatorially confined target electron energies range from $E_e \simeq 11.79$ MeV, $\sqrt{Q_e} = 24.79 Mm_e$ (point 13) down to the equatorial value of $E_e \simeq 0.539$ MeV (point 6, i.e., where the general curves meet, here $Q_e = 0$). The solid squares superimposed on the dotted curve are the PCS photon distributions using nonequatorially confined targets, specifically for 3C 279 (based on the observed luminosity spectrum). The solid squares superimposed on the solid line indicate the PCS distributions fitted to agree with observations using the f_n factors.

The values of f_1 and f_2 (not enclosed in brackets) on Table 2 are the values used in equation (23) to plot the solid squares that are superimposed on the upper dotted curve, labeled by the numbers 8 through 13 on Figure 8a; and the values of f_2 enclosed in brackets are those used in order to make the PCS distributions agree with observations. The factor f_1 tells us the fraction of the luminosity of the disk arriving at the scattering radius, and the expected angular height of the scattering regime (see eqs. [3] and [16]). The factor f_2 (as well as f_4) is defined as follows:

$$f_2 \equiv \left(\frac{\text{number of scattered photons}}{\text{total number of infalling photons}} \right);$$

thus, f_2 tells us the probability of the PCS events occurring for a distributions of infalling photons. This probability will depend on the total Klein-Nishina cross section $(\sigma_{\text{tot}})_{\text{KN}}$ for a given set of initial conditions (see Paper 1). Typical values of $(\sigma_{\text{tot}})_{\text{KN}}$ for PCS by target equatorially and nonequatorially confined electrons are $\sim 1.8 \times 10^{-25} \text{ cm}^2$ and $\sim 3.6 \times 10^{-26} \text{ cm}^2$, respectively. For comparison, $\sigma_{\text{tot}} \sim 2 \times 10^{-26} \text{ cm}^2$ for recombination to the ground state of hydrogen at $T \sim 10^9 \text{ K}$, and the geometric cross section of a nucleon is $\simeq 5 \times 10^{-25} \text{ cm}^2$.

The other model parameters on Table 2 are defined as follows: r is the scattering radius; E_e is the target electron energy; ν_{ph} is the initial infalling photon frequency; ν_{peak} and L_{peak} correspond to the points (solid squares superimposed on the dotted line) which give the continuum luminosity resulting from several distributions of PCS events (each distribution has 2000 scattering events); L_{obs} is the observed luminosity at ν_{peak} (the average frequency of the interval $\Delta\nu$ where most of the PCS photons are emitted per 2000 scattering events). Each distribution of 2000 infalling photons have monochromatic energies normalized to the power law distribution given by equation (20) for

3C 279, and by equation (21) for 3C 273. Overall, to produce the calculated Penrose luminosity spectra of Figure 8, from 56,000 (for 3C 279) to 74,000 (for 3C 273) infalling photon scattering events are used.

The solid circles on Figure 8a are due to secondary Penrose Compton scattering (SPCS; described in § 4.5.1) of low energy infalling accretion disk photons by the highly energetic PPP ($\gamma\gamma \rightarrow e^-e^+$) electrons. These SPCS processes are assumed to take place at (or near) the radius of the photon orbit ($r_{\text{ph}} \simeq 1.074M$). The energy acquired by the scattered disk photon is approximately equal to that of the target PPP ($\gamma\gamma \rightarrow e^-e^+$) electron, and thus is approximately given by equation (9). For example, a distribution of 2000 escaping PPP ($\gamma\gamma \rightarrow e^-e^+$) electron targets with energies peaked around 2.57 GeV, after undergoing SPCS, yields a distribution of 1964 escaping scattered photons with energies peaked around 2.44 GeV (point 21 on Fig. 8a). The general spectrum produced by the SPCS photons is represented by the dashed line (points 14 through 21). The peak energies of the initial PPP ($\gamma\gamma \rightarrow e^-e^+$) electron distributions (used for the targets) range from 1.289 MeV ($\gamma_e = 2.523$) to 2.469 GeV ($\gamma_e = 4.832 \times 10^3$), and the initial infalling photon distribution has monochromatic energy 0.03 MeV. To produce higher energy SPCS spectra, PPP ($\gamma\gamma \rightarrow e^-e^+$) electron distributions with larger Lorentz factors can be used. Note, the infalling incident photons (at $E_{\text{ph}} = 0.03$ MeV), assuming to originate in the accretion disk, have a luminosity power law distribution (eq. [20]) consistent with the observed spectrum of 3C 279. The solid circles superimposed on dashed line are SPCS specifically for 3C 279. The solid circles superimposed on the solid line indicate the SPCS photon distributions fitted to agree with observations using the f_n factors.

Table 3 gives the values of the factors f_1, \dots, f_5 of equation (23) used in these model calculations for 3C 279. The values of the f_n factors enclosed in brackets are those used to make the SPCS photon distributions agree with observations. The factors f_1 and f_3 give the geometric fraction of the disk luminosity intersecting the scattering radius for PPP ($\gamma\gamma \rightarrow e^-e^+$) and subsequently for SPCS, respectively. The factor f_2 , defined earlier, tells us the probability of the scattering events occurring for the given initial conditions, governed by the total pair production ($\gamma\gamma \rightarrow e^-e^+$) cross section $(\sigma_{\text{tot}})_{\gamma\gamma}$ (Paper 1). Typical values of $(\sigma_{\text{tot}})_{\gamma\gamma}$, for the PPP ($\gamma\gamma \rightarrow e^-e^+$), range from $\sim 1.7 \times 10^{-26}$ cm² to $\sim 1.3 \times 10^{-27}$ cm², for the orbiting target photon energies ranging from ~ 208 MeV to ~ 4 GeV, respectively. The factor f_4 , defined like f_2 above, tells us the probability of the SPCS events occurring for the given initial conditions, governed by the total Klein-Nishina cross section $(\sigma_{\text{tot}})_{\text{KN}}$. Typical values of $(\sigma_{\text{tot}})_{\text{KN}}$, for the SPCS, range from $\sim 2.6 \times 10^{-27}$ cm² to $\sim 2.4 \times 10^{-28}$ cm² for target PPP ($\gamma\gamma \rightarrow e^-e^+$) electron energies ranging from ~ 200 MeV to ~ 3.6 GeV, respectively. For comparison, in the photoproduction process: $\gamma p \rightarrow \pi^0 p$, σ_{tot} peaks to $\sim 3 \times 10^{-28}$ cm² at incident photon energy $E_\gamma \sim 340$ MeV, decreases to $\sim 1 \times 10^{-28}$ cm² at $E_\gamma \sim 470$ MeV, and goes to zero at $E_\gamma \lesssim 150$ MeV. The factor f_5 , which relates to the expansion rate and, thus, the core region density, gives the expected fraction of e^-e^+ pairs that undergoes SPCS, while the rest of the pairs are free to be further collimated and accelerated by a surrounding electromagnetic field.

The other model parameters on Table 3 are defined as follows: r is the scattering radius; $(E_{\mp})_{\text{peak}}$ is the energy value where most of the PPP ($\gamma\gamma \rightarrow e^-e^+$) electrons are created; ν_{peak} and L_{peak} correspond to the points which give the continuum luminosity resulting from several distributions of SPCS events [each distribution has about 2000 scattering events, depending on the number of escaping target PPP ($\gamma\gamma \rightarrow e^-e^+$) electrons]; L_{obs} is the observed luminosity at ν_{peak} (the average frequency of the interval $\Delta\nu$ where most of the SPCS photons are emitted per ~ 2000 scattering events).

On Figure 8b, for 3C 273, the dotted curve shows the general distribution for PCS by equatorially confined electrons (points 1 through 7) and by nonequatorially confined electrons (up from point 6 through 13). The solid squares for PCS, and solid circles for SPCS by PPP ($\gamma\gamma \rightarrow e^-e^+$) target electrons, are calculated specifically for 3C 273, based on the observed photon distribution. In this case, it appears that the PCS by equatorially confined target electrons contributes a significant part to the X-ray regime of the observed spectrum (indicated by points 2 through 5 above the observed curve). The solid squares at point 2 and points 3 through 5 are for PCS by equatorially confined targets at $r = 1.099M$ and $r_{\text{mb}} = 1.089M$, respectively; and points 8 through 13 superimposed on the dotted curve in the soft γ -ray regime, directly above the observed spectrum, are for PCS by nonequatorially confined orbiting targets at r_{mb} . The solid squares superimposed on the solid line indicate the PCS distributions (for the corresponding labeled points lying directly above) that have been fitted to agree with observations using the f_n factors. Table 4 gives the values of the factors f_1 and f_2 of equation (23) used in these model calculations for 3C 273. The values of the f_n factors enclosed in brackets are the values used to make the PCS distributions to agree with observations. Note that, the parameters of the columns on Table 4 are defined as on Table 2.

Further, on Figure 8b, recall that the solid circles are due to SPCS of infalling accretion disk photons by the PPP ($\gamma\gamma \rightarrow e^-e^+$) electrons. These SPCS processes are assumed to take place at (or near) the radius of the photon orbit r_{ph} . The general spectrum resulting from SPCS is represented by the dashed line. The target electron distributions, resulting from the PPP ($\gamma\gamma \rightarrow e^-e^+$), used in these SPCS processes, have peak energies ranging from 1.289 MeV ($\gamma_e = 2.523$) to 2.469 GeV ($\gamma_e = 4.832 \times 10^3$), and the infalling incident photon distributions have monochromatic energy $E_{\text{ph}} = 0.03$ MeV. The solid circles superimposed on the dashed line indicate SPCS photon distributions specifically for 3C 273. The solid circles superimposed on the solid lines indicate the SPCS photon distributions that have been fitted to agree with observations using the f_n factors (for each of the corresponding labeled points lying directly above). Table 5 gives the values of the f_n factors (f_1, \dots, f_5) of equation (23) used in these model calculations for 3C 273. The values of the f_n factors enclosed in brackets are the values used to make the SPCS photon luminosity agree with observations. Note that, the parameters of the columns on Table 5 are defined as they are on Table 3.

From Figure 8, one can clearly see that luminosities due to Penrose processes in the high energies regime are sufficient to explain the observations of these quasars. Importantly, the Penrose mechanism generates an abundance of energy, such that it allows for the smallness in the cross

sections at high energies. Moreover, notice that, the generated luminosity spectra produced by the PCS and PPP ($\gamma\gamma \rightarrow e^-e^+$) fall off in regions consistent with the gaps in the radiation of the general observed spectra of AGNs.

Now returning to Figures 1a and 8a to discuss the total observed spectrum of 3C 279: In general, the radio/mm emission may be due to the interaction of a magnetic field B , say of the accretion disk ($B_d \sim 10^2$ gauss), with electrons of the disk or PPP ($\gamma\gamma \rightarrow e^-e^+$) electrons. For example, for electrons with energies between $\sim 1.8 - 13$ MeV, the synchrotron frequency of the emitted photons will be $\nu_{\text{syn}} \sim 5.2 \times 10^9 - 2.7 \times 10^{11}$ Hz, where $\nu_{\text{syn}} \sim 4 \times 10^6 \gamma_e^2 B$ (Burbidge, Jones, & O’Dell 1974). The infrared to UV emission spectrum can be produced by the PPP ($\gamma\gamma \rightarrow e^-e^+$) electrons at $B_d \sim 10^2$ gauss, i.e., for electrons having energies between $\sim 30 - 2000$ MeV, the synchrotron frequency of the emitted photons will be $\nu_{\text{syn}} \sim 1.5 \times 10^{12} - 6.4 \times 10^{15}$ Hz. Of course Eilek’s (1980) e^-e^+ pairs, with energies peaking ~ 35 MeV, could also contribute synchrotron radiation to the spectrum in this regime. Moreover, the accretion disk radiates thermal photons in this region of the spectrum, with maximum radiation peaking from $\sim 2 \times 10^{14}$ to 2×10^{15} Hz. This thermal radiation is due to viscosity in the disk as angular momentum is transferred outward, thereby heating the disk, producing copious photons. Particularly, in the optical band, this is most likely the dominant observed emission for “normal” quasars, but not for OVV quasars, like 3C 279. For the case of OVV quasars, the observed optical emission is probably dominated by synchrotron emission in the jet, since, in these sources, the jet is believed to be pointed in a direction near the observer’s line of sight; this gives rise to observed features, such as intense variability and high polarization in the optical emission. The X-ray emission ($\sim 1.3 - 41$ keV) can be produced by both PCS and the inner region of a thin disk/ion corona accretion. In general, for a $10^8 M_\odot$ KBH, the PCS has emission over the total X-ray band, and so does the inner region of the accretion disk. However, from comparing Figure 8a, the accretion disk appears to be the more dominant mechanism in producing the observed X-ray emission of 3C 279 (i.e., if we limit the photons participating in the PCS to be only those from the observed soft X-ray spectrum we believe to be disk radiation). On the other hand, as mentioned earlier, the X-ray emission may be predominantly beamed PCS. This is not the case for 3C 273 (compare Fig. 8b; more on this below). The soft γ -ray emission can be produced by infalling X-ray photons ~ 30 keV ($\sim 3.5 \times 10^8$ K) from a thin disk/ion corona accretion; such infalling disk X-rays can first undergo PCS (see Fig. 3a), producing photons that can populate the photon orbit for PPP ($\gamma\gamma \rightarrow e^-e^+$) (Williams 2002a, 2002b); these pairs can subsequently undergo SPCS with additional infalling disk photons, producing γ -rays in the range $\sim 1 - 27$ MeV, peaking in luminosity at ~ 15 MeV (or $\sim 3.6 \times 10^{21}$ Hz). The soft γ -ray emission can also be produced directly by the PCS photons (see Figs. 2 and 3b), with energies extending up to, say, ~ 13 MeV (or $\sim 3 \times 10^{21}$ Hz). The cutoff of the observed soft γ -ray emission is probably due to the inability of prior PCS to populate the photon orbit—for PPP (leading to SPCS), and/or the inability, or unavailability, of higher energy electrons to populate the nonequatorially confined target particle orbits—for PCS [from ion corona nuclear reaction processes (§§ 4.2.2 and 4.4)]. The higher energy γ -ray emission [up to ~ 4 GeV ($\sim 10^{24}$ Hz)] can be produced exclusively by the PPP ($\gamma\gamma \rightarrow e^-e^+$) electrons (i.e., after some of the PPP electrons have undergone SPCS processes).

These processes can contribute copious photons to the observed γ -ray emission spectrum, and is probably responsible for the large luminosities at very high energies (compare Figs. 1a and 8a). Any observable fall off in the hard γ -ray regime is probably due to the increasingly smaller cross section at higher energies. Note, it appears that the γ -rays produced by the $\pi^0 \rightarrow \gamma\gamma$ decays (§§ 4.2.2 and 4.4), satisfying conditions to populate the photon orbit for PPP ($\gamma\gamma \rightarrow e^-e^+$), can safely be predicted to have energies > 1.6 MeV, based on observations: such γ -rays will acquire gravitational blueshifted energies > 85 MeV, with expected Q values $> 6M^2m_e^2$.

If the radiation is preferentially beamed towards us, we will overestimate the true luminosity and energy, depending on the observing angle, θ_s (§ 4.5.2). This does not pose a problem for this present model, because the luminosity and energy could undergo an apparent shift and still be described by these Penrose processes. Moreover, according to equations (11) through (14), if the observing angle is $\theta_s = 15^\circ$, and the Lorentz factor of the blob is $\Gamma = 12$, implying a Doppler boost of $\delta_* \simeq 2.2$, then the energy will shift by a factor of $\simeq 2.2$ (increasing from an intrinsic energy of, say, ~ 1.8 GeV to an apparent energy of ~ 4 GeV), and the intrinsic luminosity shifts upward by a factor of $\simeq 15.8$, with $m = 3.5$, to its observed value. The apparent velocity would be $\simeq 6.9c$, consistent with observations ($v_{\text{app}} \simeq 6.9c$ for 3C 279; Porcas 1987), and, for completion, the intrinsic size of the emitting region, say in the γ -ray > 100 MeV (§ 3.2)—for a variability time scale of \sim a day, will be $\bar{R} \sim 0.002 \text{ pc} \sim 195 r_g$, where $r_g (= 2MG/c^2)$ is the so-called gravitational radius.

Referring now to Figures 1b and 8b, to discuss the total observed spectrum of 3C 273: The emission in the radio to UV region of the spectrum can probably be explained by the same processes as described above for 3C 279, i.e., Penrose, accretion disk, and synchrotron emission processes. In the X-ray regime, particularly, from ~ 3.5 to 207 keV ($\sim 10^{18}$ to 5×10^{19} Hz), the emission spectrum is probably produced by PCS and the inner region of an ion corona accretion disk (compare Fig. 8b). Since the X-ray emission extends to much greater than ~ 3.5 keV, which is the maximum energy produced by the inner region of a thin disk, then we conclude that the ion corona and PCS are most likely producing the hard X-rays. Since the accretion can exist in either or both of two phases: thin disk and/or ion corona, and can remain in any of these phases for an indefinite time, depending on the cooling mechanism, it is possible that quasar 3C 273 is spending its “lifetime” largely in the ion corona/hot torus (or the ADAF) phase. This is contrary to 3C 279, which, as observations suggest, spends its lifetime oscillation between the thin disk and ion corona phases, on a relatively small timescale (further comparisons of the spectra of 3C 279 and 3C 273 are presented in the following section).

An explanation for the observed γ -ray emission spectrum is as follows (compare Fig. 8b). The γ -ray emission from ~ 1 to 13 MeV ($\sim 2 \times 10^{20}$ to 3×10^{21} Hz) is most likely due to a mixture of PCS and relativistic SPCS by the PPP ($\gamma\gamma \rightarrow e^-e^+$) electrons, as described above for the soft γ -ray emission in 3C 279. The γ -ray emission from ~ 13 MeV up to ~ 4 GeV is probably due predominantly to SPCS. Some of the γ -ray emission, at least in the regions between ~ 35 –100 MeV, may be due to Eilek’s particles (§ 4.4), as indicated in Figure 1b. Finally, relativistic beaming may

serve to boost the overall γ -ray emission, depending on the observing angle, since superluminal motion has been detected in observations of 3C 273 (Porcas 1987).

5.3. The Compared Spectra of 3C 279 and 3C 273

Now we compare further the spectra of 3C 279 and 3C 273, again using Figures 1 and 8. The classification of these quasars as radio loud is evident from their spectra in the radio/mm region. The shape of the spectrum of 3C 273 looks like the “enhanced” spectrum of 3C 279, except for the higher luminosities in 3C 279 and the radio tail in 3C 273. The higher luminosity and the lack of a radio tail in 3C 279 is probably largely due to the radiation of 3C 279 being beamed more in the direction of the observer than the radiation of 3C 273. Therefore, the spectrum of 3C 279 has been Doppler (i.e., apparently) blueshifted to a higher energy interval, and the luminosity has been apparently increased (§ 4.5.2). This is consistent with radio observations which detect more superluminal motion (or relativistic beaming near the line of sight of the observer) in 3C 279 than in 3C 273 (Porcas 1987). Next, notice on the schematic broad band spectral diagrams of 3C 279 and 3C 273 (Fig. 1), the region which I have labeled as the “inner accretion disk,” the emission of 3C 273 is hotter, covering a broader band of emission than 3C 279. This to be expected if 3C 273 is in a predominantly ion torus (or advection dominated) state, as opposed to 3C 279 (which appears to oscillates in a highly variable fashion between the thin disk and ion corona phases—for this reason 3C 279 is classified as an OVV quasar). Moreover, the hotter state of the accretion disk (ion torus), which is heated by a runaway thermal instability (§ 4), would result in enhanced Penrose processes [PCS and PPP ($\gamma\gamma \rightarrow e^-e^+$)] and enhanced synchrotron radiation due to the presence of more relativistic electrons and γ -ray photons. This appears to be the case always in the continuum emission of 3C 273 and sometimes in the emission spectrum of 3C 279, with 3C 279 not quite achieving the full ion torus status of 3C 273 (compare Fig. 1). Thus in summary, the differences in the spectra of 3C 279 and 3C 273 are probably due to (1) the more beaming effect in 3C 279, and (2) the predominantly ion torus phase of 3C 273.

5.4. Radio Loud and Radio Quiet Quasars

The results of these Penrose processes allow one to make a brief statement on the evolution of radio loud and radio quiet quasars. Since radio loud galaxies are usually associated with large elliptical galaxies with radio lobes, and assuming that quasars are progenitors of at least some galaxies (particularly nearby AGNs), it is perhaps safe to say that radio loud galaxies evolve from radio loud quasars. This is based on observations and the model presented in this paper, suggesting that radio loud quasars have geometrically larger, more effective ion tori (or coronas) than their counterparts, radio quiet quasars, which probably possess cooler thin disks with small coronas (if any). The hot thick disks proposed for radio loud quasars are expected to contain more relativistic electrons ($\gtrsim m_e c^2$), thus leading to more synchrotron radiation in the radio, and the geometric

thickness possibly creates the environment for funneling and collimating the emitted particles into jets (as it appears to be the cases for 3C 279 and 3C 273). So, in this scenario, radio loud quasars, which are believed to possess ion tori, eventually evolve into “bright” elliptical galaxies; and the degree of radio loudness will depend on the phase of the stabilizing mode of the ion torus. Now on the other hand, radio quiet galaxies are usually associated with spiral galaxies, in which large-scale collimated radio jets are absent (Kotanyi, Hummel, & van Gorkom 1987). However, observations of spiral galaxies show some evidence of radio emission strictly confined to the optical disk. These observations are consistent with the model presented in this paper. This model suggests that radio quiet quasars may have thin disks, as mentioned above, with geometrically smaller ion coronas, if any, than radio loud quasars. This suggestion implies that radio quiet quasars eventually evolve into bright spiral galaxies, with radio and optical emission being confined to the disk. That is, without the presence of a geometrically larger ion torus to perhaps maintain the collimation of the jet as in radio loud quasars (the initial collimation due to Penrose processes may not be able to do it alone), a radio quiet quasar results, which may eventually evolve into an AGN-type spiral galaxy, lenticular galaxy, or maybe even elliptical galaxy, depending on the size of the geometrically smaller ion torus.

6. CONCLUSION AND FUTURE WORK

I have presented a model that can possibly explain the observed features in the continuum spectra of 3C 279 and 3C 273: using Penrose processes [PCS and PPP ($\gamma\gamma \rightarrow e^-e^+$)], a thin disk/ion corona (or ADAF), and a magnetic field strength ($\sim 10^2$ gauss) like that typically assumed for an accretion disk surrounding a KBH. I have demonstrated that the general spectra of AGNs in the high energy regime can be explained by this model with or without evoking relativistic beaming. This makes this model feasible to explain the general emission spectrum of any AGN, irrespective of the observing angle, whereas, many other models to date must rely on relativistic beaming. Now, when relativistic beaming is observed to be important, such as through superluminal motion, then it can be incorporated into the modeling of the source to reproduce its unique spectrum. For example, relativistic beaming seems to be more important in 3C 279 than in 3C 273. That is, when relativistic beaming is included in the modeling of these sources, and 3C 279 is given a smaller observing angle relative to the axis of the jet, it increases the observed luminosity and energy relative to the spectrum of 3C 273; this is consistent with what we observe (compare the γ -ray luminosities of Figs. 1a and 1b).

Moreover, when relativistic beaming is included and a power law spectrum for the protons in ADAFs is assumed, which can yield γ -rays due to the π^0 decays with energies ~ 2 GeV (Mahadevan et al. 1997), this present model, using the PPP ($\gamma\gamma \rightarrow e^-e^+$) and such γ -rays, can explain the \sim TeV γ -ray observations of the blazar Mrk 421. For example, when the blueshift at the photon orbit is taken into account for these π^0 -induced γ -rays, the PPP ($\gamma\gamma \rightarrow e^-e^+$) can yield Lorentz factors as high as $\gamma_e \sim 10^5$ for the blobs. If we choose Γ to be ~ 25 (see eqs. [10] to [14]), such

blobs when viewed at an observing angle $\sim 1^\circ$ will emit γ -rays with apparent energies ~ 2 TeV.

Importantly, the model presented here applies to all mass size black holes, which includes stellar mass black holes as well. For example, the observations of the classical stellar/galactic black-hole candidate Cygnus X-1, the bright Seyfert 1 galaxy MCG—6-30-15, and the active giant elliptical galaxy M87 can all be explained by these Penrose processes [see Williams (2002b) for qualitative descriptions].

Details of the collimating effects of these Penrose processes, and accelerating processes due to the associated electromagnetic field, which can possibly extend the jets out to very large distances, will be investigated in future work by the author. Further, local acceleration due to strong shocks, similar to the models suggested by Blandford and Eichler (1987), may be important also as the jets expand relativistically outward. Such models should be investigated using the distributions of these Penrose scattered particles.

In addition, I have argued in this paper that instability in the accretion disk, which can cause the disk to vary between thin disk and ion corona (or hot torus) phases, plays a significant role in determining the morphology of quasars, possibly creating the two general classes: radio loud and radio quiet quasars. It is probable that such quasars eventually evolve into radio loud and radio quiet galaxies. However, these suggestions need to be investigated further.

Finally, I point out, the consistency of this present model with observations of black hole sources, in general, shows its universal application: suggesting it to be a complete theory in the extraction of energy-momentum from a black hole.

First, I thank God for His thoughts and for making this research possible. Next, I wish to thank Dr. Henry Kandrup and Dr. Fernando de Felice for helpful comments and discussions. Also, I thank Dr. Roger Penrose for his continual encouragement. Finally, hospitality at the University of Florida and North Carolina A & T State University is gratefully acknowledged. This work was supported in part by the National Research Council Ford Foundation, Bennett College Women's Leadership Institute, and a grant from the American Astronomical Society.

APPENDIX

As referenced in the main text, examples of results of Williams (Paper 1; 2002b) being duplicated are discussed in the following items:

1. Gammie (1999) and Krolik (1999) present black hole physics (in varying degrees) already presented in Williams' (Paper 1) Penrose process analysis, particularly, (a) the general method used to extract energy, (b) the final resulting equations due to inertial frame dragging showing that energy is extracted, (c) the knowledge of the existence of particle orbits in the ergosphere inside the radius of marginal stability r_{ms} , and (d) application of the general conserved energy E and

azimuthal momentum L parameters as they relate to the particle’s orbit, inside the ergosphere, in a Kerr metric (see Appendix A of Paper 1), in their effort to make the Blandford-Znajek (1977) type models work. Specifically, they consider a magnetic torque being applied to the disk particles at $r \lesssim r_{\text{ms}}$ (Krolik 1999).

In Gammie’s (1999) investigation, of the MHD version of the Penrose effect, proposed by Takahashi et al. (1989), he defines an “efficiency” of magnetic accretion:

$$\epsilon^B \equiv \frac{F_M - F_E}{F_M} \equiv \frac{(-1) - F_E}{(-1)} = 1 + F_E > 1, \quad (1)$$

for $F_E > 0$, implying that energy is extracted, where F_M , normalized to -1 (in his calculations), is defined as the conserved “rest mass flux,” indicating an *assumed* constant inward flux of negative energy particles into the black hole due to the torque of the *presumed* nonnegligible accretion disk magnetic field at $\sim r_{\text{ms}}$; and F_E is the conserved mass-energy flux, which in general is positive inside the ergosphere, i.e., at least if it is to escape to infinity. Now, the general expression for the efficiency of the release of gravitational binding energy due to accretion of a unit of rest mass m_o is

$$\epsilon \equiv \frac{E_{\text{rad}}}{E_{\text{tot}}} = \frac{\gamma m_o c^2 - E}{\gamma m_o c^2}, \quad (2)$$

where E is the conserved orbital energy parameter as measured by an observer at infinity, E_{rad} is the energy radiated to infinity, and E_{tot} is the total energy of the infalling mass. Note, $\epsilon \simeq 0.42$ for a maximum rotating ($a = M$) KBH at r_{ms} (neglecting energy released due to viscosity). If ϵ is > 1 , this would imply that $E_{\text{rad}} > E_{\text{tot}}$, indicating that rotational energy is extracted from the black hole. This would only occur if the total infall energy is negative or for $E < 0$, thus the reason why Gammie set $F_M = -1$ (compare eq. [A1]). Not surprisingly, in Gammie’s (1999) proposed simplified so-called MHD Penrose model, it was found that $\epsilon^B \approx 1.04$, particularly when we see below how he determined F_E . But, the fact that rotational energy can be extracted due to the Penrose mechanism had already been shown in details in Williams’ (1991, Paper 1) theoretical: analytic and numerical calculations of realistic astrophysical Penrose processes in the ergosphere of a KBH [see §§ II.C, IV.A.1.e, IV.D, eq. (2.31), and Table II of Williams (Paper 1)]. The efficiency to show whether or not rotational energy is extracted in a “classical Penrose process” (i.e., resulting in negative energy infall) as opposed to a “quasi-Penrose process” (Paper 1; see also § 4.2.1 of this present manuscript) is given by (Williams 1991, Paper 1; Piran & Shaham 1977)

$$\epsilon^{\text{PS}} \equiv \frac{E_3 - (E_1 + E_2)}{E_1 + E_2}, \quad (3)$$

where the subscripts 1, 2, and 3 indicate the infalling particle, the orbiting target particle, and the scattered escaping particle, respectively. For $\epsilon^{\text{PS}} > 0$, rotational energy is extracted in the scattering event by a classical Penrose process. It is found that ϵ^{PS} acquires values up to ~ 1.6 , for escaping particle distributions, without the need to include the magnetic field of the accretion disk (see Paper 1 for details). Nevertheless, it has been shown by Wagh, S. M., Dhurandhar, S. V., &

Dadhich (1985); Parthasarathy et al. (1986) that electromagnetic fields can increase the efficiency of fission and nonrelativistic Penrose processes.

The expression that Gammie (1999) uses to eliminate two degrees of freedom by expressing F_E in terms of F_L and by fixing Ω_F , the angular velocity of a magnetic field line (Takahashi et al. 1990), can be derived using the initial conditions and the final results of my Penrose analysis (Paper 1). For example, Gammie defines Ω_F by the angular velocity of the orbiting fluid at constant r (i.e., $u^r = 0$), where u^μ is the 4-velocity. He (a) assumes that $\Omega_F \approx \omega_{\text{ms}}$, where ω_{ms} defines the inertial frame dragging velocity at r_{ms} ; (b) assumes that the “fluid,” being torqued by the magnetic field at r_{ms} , resulting in a radial inflow of negative energy flux, initially orbits at a constant radius ($u^r = 0$), just as I initially assume that my target particles orbit at constant r , with conserved energy E and azimuthal angular momentum L as measured by an observer at infinity, given analytically by Bardeen et al. (1972) and Williams (Paper 1, 2002b) for equatorially and nonequatorially confined particle orbits, respectively. The final expression of the energy of particles escaping due to Penrose scattering events [see eqs. (3.47) and (3.89) of Paper 1], can be adjusted to “fit” Gammie’s problem: That is,

$$E' = e^\nu \varepsilon' + \omega e^\psi (p')_\Phi \quad (4)$$

$$\begin{aligned} &= e^\nu \varepsilon' + \omega L' \\ &= (E - \omega L) + \omega L', \end{aligned} \quad (5)$$

where the primes indicate final conditions. The transformation of the energy from the local nonrotating frame to the Boyer-Lindquist coordinate frame [eq. (2.8d) of Paper 1], and the assumption that energy-momentum flux be continuous across the boundary between the inflow and the disk (Gammie 1999) (i.e., $\varepsilon = \varepsilon'$ as measured by a local nonrotating frame observer) have been used. Let $E \equiv \tilde{E}m_o$, $L \equiv \tilde{L}m_o$, with $\Omega_F \equiv \omega$, where m_o is the particle’s rest mass, then equation (5) becomes

$$E' = (\tilde{E} - \Omega_F \tilde{L})m_o + \Omega_F L'.$$

To express the above equation as the flux equation given by Gammie (1999, p. L58), we multiply both sides by per unit (length)² per unit time to obtain the desired equation:

$$F_E = (\tilde{E} - \Omega_F \tilde{L})F_M + \Omega_F F_L, \quad (6)$$

where the guiding center approximation has been used (de Felice & Carlotto 1997; de Felice & Zonotti 2000; see also Williams 2002b). Notice that Gammie (1999, p. L58) merely states the above equation without saying anything about its derivation (nor where it came from), except that “one can show” this to be true. He then uses this equation to solve a system of three equations: $\partial_{u^r} F_E(r_f, u_f^r, F_L) = 0$, $\partial_r F_E(r_f, u_f^r, F_L) = 0$, $F_E(r_f, u_f^r, F_L) - F_E(r_{\text{ms}}, 0, F_L) = 0$, using the conservation of energy, to be solved numerically for the three unknowns, F_L and the fast critical points (r_f, u_f^r) . He thus finds in some cases that $F_L > 0$ and $F_E > 0$; this is no surprise since it appears he used results derived from radially infalling particles, colliding with the orbiting target particles

(Paper 1), only altering them to express results for, instead, a radially directed magnetic field, assumed to torque the orbiting “target” particles, causing them to have negative, retrograde energy orbits, for which he represents as a negative “rest mass flux” [$F_M \approx -\dot{M}r/(2H)$] normalized to be -1 . To find that $F_L > 0$ and $F_E > 0$, from my results (Paper 1), as modified by Gammie, simply means that negative particle energy is falling into the KBH, resulting in positive particle energy and angular momentum being extracted. However, from his results one can not tell if, or how, the magnetic field torques the particles, putting them on negative energy plunges. Only a microphysical analysis, such as that done by Williams (Paper 1), for Penrose scattering processes, will determine what effect the magnetic field has on the orbiting test particles. If Gammie (1999) and Krolik (1999) are proposing that the magnetic torque, acting on the orbiting particles, can serve the same purpose as infalling particle collisions with the orbiting target particles (Paper 1), then the task concerning these Blandford-Znajek type models would be to show in details this to be true, i.e., applying the microphysics involved, including the Lorentz force on a particle in the local frame, to assess the effectiveness of magnetic-particle interactions. This has somewhat been addressed by Li (2003), as discussed in item 2 below.

2. The relationship between the local velocity of the particle, the conserved specific azimuthal angular momentum (L/m_o) and specific energy (E/m_o), presented by Li [2003: eqs. (24), (25) and (26)] for *fluid* particles are just those previously derived by Williams for *single* particles [Paper 1: eqs. (3.15a) and (3.15b)] and the particle azimuthal circular velocity presented by Bardeen, Press, & Teukolsky [1972: eq. (3.10)]. Moreover, Li (2003) finds that the dynamical effects of the magnetic field are negligible, in the region $r < r_{\text{ms}}$, inside the ergosphere, as previously suggested by Williams (2002b), contrary to that proposed by Gammie (1999) and Krolik (1999).

REFERENCES

- Abramowicz, M. A., Chen, X.-M., Granath, M., & Lasota, J.-P. 1996, ApJ, 471, 762
- Abramowicz, M. A., Chen, X.-M., Kato, S., Lasota, J.-P., & Regev, O. 1995, ApJ, 438, L37
- Abramowicz, M. A., Czerny, B., Lasota, J. P., & Szuszkiewicz, E. 1988, ApJ, 332, 646
- Balbus, S. A., & Hawley, J. F. 1991, ApJ, 376, 214
- Bardeen, J. M., Press, W. H., & Teukolsky, S. A. 1972, ApJ, 178, 347
- Barthel, P. D., in Superluminal Radio Sources, eds. J. A. Zensus and T. J. Pearson (Cambridge University Press, Cambridge), 148
- Bassani, L., & Dean, A. J. 1981, Nature, 294, 332
- Bassani, L., Dean, A. J., Di Cocco, G., & Perotti, F. 1985, in Active Galactic Nuclei, ed. J. E. Dyson (Manchester, Manchester Univ. Press), 252

- Bertsch, D. L., et al. 1993, *ApJ*, 405, L21
- Bini, D., Cherubin, C., Jantzen, R. T., & Mashhoon, B. 2002, *Class. Quantum Grav.*, 2, 457
- Bičák, J. 2000, *Pramana*, 55, No. 4, 481 (gr-qc/0101091)
- Bičák, J. & Ledvinka, T. 2000, *IL Nuovo Cimento*, 115 B, 739 (gr-qc/0012006)
- Biretta, J. A., Sparks, W. B., & Macchetto, F. 1999, *ApJ*, 520, 621
- Blandford, R. D., & Eichler, D. 1987, *Phys. Rep.*, 154, 1
- Blandford, R. D., & Königl, A. 1979, *ApJ*, 232, 34
- Blandford, R. D., & Levinson, A. 1995, *ApJ*, 441, 79
- Blandford, R. D., & McKee, C. F. 1977, *MNRAS*, 180, 343
- Blandford, R. D., McKee, C. F., & Rees, M. J. 1977, *Nature*, 267, 211
- Blandford, R. D., & Znajek, R. L. 1977, *MNRAS*, 179, 433
- Boyer, R. H., & Lindquist, R. W. 1967, *J. Math. Phys.*, 8, 265
- Burbidge, G. R., Jones, T. W., & O'Dell, S. L. 1974, *ApJ*, 193, 43
- Carter, B. 1968, *Phys. Rev.*, 174, No. 5, 1559
- Carter, B. 1973, in *Black Holes*, ed. C. DeWitt, & B. S. DeWitt (New York: Gordon and Breach Science Publishers), 57
- Chen, X., & Taam, R. E. 1996, *ApJ*, 466, 404
- Christodoulou, D. 1970, *Phys. Rev. Lett.*, 25, No. 22, 1596
- Cohen, M. H., et al. 1977, *Nature*, 268, 405
- de Felice, F., & Calvani, M. 1972, *IL Nuovo Cimento*, 10 B, 447
- de Felice, F., & Carlotto, L. 1997, *ApJ*, 481, 116
- de Felice, F., & Curir, A. 1992, *Class. Quantum Grav.*, 9, 1303
- Dennett-Thorpe, J., Bridle, A. H., Scheuer, P. A. G., Laing, R. A., & Leahy, J. P. 1997, *MNRAS*, 289, 753
- Dermer, C. D., & Schlickeiser, R. 1993, *ApJ*, 416, 458
- Dermer, C. D., Schlickeiser, R., & Mastichiadis, A. 1992, *A&A*, 256, L27

- Eardley, D. M., & Lightman, A. P. 1975, *ApJ*, 200, 187
- Erber, T. 1966, *Rev. Mod. Phys.*, 38, No.4, 626
- Eilek, J. A. 1980, *ApJ*, 236, 664
- Eilek, J. A. 1988, in *Supermassive Black Holes*, ed. M. Kafatos (New York: Cambridge Univ. Press), 243
- Eilek, J. A. 1991, private communication
- Eilek, J. A. 1999, in *The Radio Galaxy Messier 87*, ed. H.-J. Röser & K. Meisenheimer (Germany: Springer-Verlag), 324
- Eilek, J. A., & Kafatos, M. 1983, *ApJ*, 271, 804
- Elvis, M. 1988, in *Supermassive Black Holes*, ed. M. Kafatos (New York: Cambridge Univ. Press), 131
- Esin, A. A., McClintock, J. E., & Narayan, R. 1997, *ApJ*, 489, 865
- Fichtel, C. E. 1992, talk presented at the 16th Texas Symposium on Relativistic Astrophysics and the 3rd Symposium on Particles, Strings, and Cosmology (Berkeley)
- Fichtel, C. E. 1993, in *Texas/PASCOS 92: Relativistic Astrophysics and Particle Cosmology*, ed. C. W. Akerlof & M. A. Srednicki (New York: New York Academy of Sciences), 136
- Filippenko, A. V. 1988, in *Supermassive Black Holes*, ed. M. Kafatos (New York: Cambridge Univ. Press), 104
- Gammie, C. F. 1999, *ApJ*, 522, L57
- Hartman, R. C., et al. 1992, *ApJ*, 385, L4
- Hawley, J. F., & Balbus, S. A. 1991, *ApJ*, 376, 223
- Hermesen, W., et al. 1993, *A&AS*, 97, 97
- Hirokuni, K., & Okamoto, I. 1998, *ApJ*, 497, 563
- Hjellming, R. M., & Rupen, M. P. 1995, *Nature*, 375, 464
- Hunter, S. D., et al. 1993, *ApJ*, 409, 134
- Isobe, T., Feigelson, E. D., Singh, K. P., & Kembhavi, A. 1988, in *Supermassive Black Holes*, ed. M. Kafatos (New York: Cambridge Univ. Press), 162
- Jones, D. L., in *Superluminal Radio Sources*, eds. J. A. Zensus and T. J. Pearson (Cambridge University Press, Cambridge), 148

- Jones, T. W. 1988, in *Supermassive Black Holes*, ed. M. Kafatos (New York: Cambridge Univ. Press), 59
- Jones, T. W., & Tobin, W. 1977, *ApJ*, 215, 474
- Junor, W., Biretta, J. A., & Livio, M. 1999, *Nature*, 401, 891
- Kafatos, M. 1980, *ApJ*, 236, 99
- Kafatos, M., & Leiter, D. 1979, *ApJ*, 229, 46
- Kerr, R. P. 1963, *Phys. Rev. Lett.*, 11, 237
- Kotanyi, C., Hummel, E., & van Gorkom, J. 1983, in *Astrophysical Jets*, ed. A. Ferrari & A. G. Pacholczyk (Dordrecht: D. Reidel Publishing Co.), 97
- Krolik, J. H. 1999, *ApJ*, 515, L73
- Leiter, D., & Kafatos, M. 1978, *ApJ*, 226, 32
- Li, L.-X. 2002, *ApJ*, 567, 463
- . 2003, *Phys. Rev. D*, 67, 044007 (astro-ph/0212456)
- Liang, E. P. 1998, *Phys. Rep.*, 302, 67
- Lightman, A. P. 1974a, *ApJ*, 194, 419
- . 1974b, *ApJ*, 194, 429
- Lightman, A. P., & Eardley, D. M. 1974, *ApJ*, 187, L1
- Lovelace, R. V. E. 1976, *Nature*, 262, 649
- Mahadevan, R., Narayan, R., & Krolik, J. 1997, *ApJ*, 486, 268
- Maraschi, L., Ghisellini, G., & Celotti, A. 1992, *ApJ*, 397, L5
- Marscher, A. P. 1978, *ApJ*, 219, 392
- Mirabel, I. F., & Rodriguez, L. F. 1996, in *Solar and Astrophysical Magnetohydrodynamic Flows*, ed. K. C. Tsinganos (Netherlands: Kluwer Academic Publishers), 683
- . 1998, *Nature*, 392, 673
- Misner, C. W., Thorne, K. S., & Wheeler, J. A. 1973, *Gravitation* (New York: W. H. Freeman and Company)
- Mushotzky, R. F. 1988, in *Supermassive Black Holes*, ed. M. Kafatos (New York: Cambridge Univ. Press), 143

- Narayan, R. 1997, private communication
- Narayan, R. et al. 1998, *ApJ*, 492, 554
- Narayan, R., Kato, S., & Honma, F. 1997, *ApJ*, 476, 49
- Narayan, R., & Yi, I. 1994, *ApJ*, 428, L13
- . 1995, *ApJ*, 452, 710
- Novikov, I. D., & Thorne, K. S. 1973, in *Black Holes*, ed. C. DeWitt & B. S. DeWitt (New York: Gordon and Breach Science Publishers), 343
- Page, D. N., & Thorne, K. S. 1974, *ApJ*, 191, 499
- Parthasarathy, S., Wagh, S. M., Dhurandhar, S. V., & Dadhich, N. 1986, *ApJ*, 307, 38
- Penrose, R. 1969, *Rivista Del Nuovo Cimento: Numero Speciale*, 1, 252
- Piran, T., & Shaham, J. 1977a, *Phys. Rev. D*, 16, No. 6, 1615
- . 1977b, *ApJ*, 214, 268
- Piran, T., Shaham, J., & Katz, J. 1975, *ApJ*, 196, 107
- Porcas, R. W. 1987, in *Superluminal Radio Sources*, ed. J. A. Zensus & T. J. Pearson (Cambridge: Cambridge Univ. Press), 12
- Punch, M., et al. 1992, *Nature*, 358, 477
- Punsly, B. 1991, *ApJ*, 372, 424
- Punsly, B. 1996, *ApJ*, 467, 105
- Punsly, B., & Coroniti, F. V. 1989, *Phys. Rev. D*, 40, No. 12, 3834
- . 1990a, *ApJ*, 350, 518
- . 1990b, *ApJ*, 354, 583
- Rees, M. J., Begelman, M. C., Blandford, R. D., & Phinney, E. S. 1982, *Nature*, 295 17
- Regge, T., & Wheeler, J. A. 1957, *Phys. Rev.*, 108, 1063
- Schmidt, M. 1992, talk presented at the 16th Texas Symposium on Relativistic Astrophysics and the 3rd Symposium on Particles, Strings, and Cosmology (Berkeley)
- Shakura, N. I., & Sunyaev, R. A. 1973, *A&A*, 24, 337
- Shapiro, S. L., Lightman, A. P., & Eardley, D. M. 1976, *ApJ*, 204, 187

- Sikora, M., Begelman, M. C., & Rees, M. J. 1994, *ApJ*, 421, 153
- Stecker, F. W., de Jager, O. C., & Salamon, M. H. 1996, *ApJ*, 473, L75
- Stern, D., et al. 2000, *ApJ*, 533, L75
- Sturrock, P. A. 1971, *ApJ*, 164, 529
- Sturrock, P. A., Petrosian, V., & Turk, J. S. 1975, *ApJ*, 196, 73
- Takahashi, M., Nitta, S., Tatematsu, Y., & Tomimatsu, A. 1990, *ApJ*, 363, 206
- Thirring, H., & Lense, J. 1918, *Phys. Z.*, 19, 156
- Thorne, K. S. 1974, *ApJ*, 191, 507
- Thorne, K. S., & Price, R. H. 1975, *ApJ*, 195, L101
- Thorne, K. S., Price, R. H., & Macdonald, D. A. 1986, *Black Holes: The Membrane Paradigm* (New Haven: Yale University Press)
- Unwin, S. C., Cohen, M. H., Biretta, J. A., Hodges, M. W., & Zensus, J. A. 1989, *ApJ*, 340, 117
- von Montigny, C., et al. 1993, *A&AS*, 97, 101
- Wagh, S. M., Dhurandhar, S. V., & Dadhich, N. 1985, *ApJ*, 290, 12
- Weekes, T. C. 1993, in *Texas/PASCOS 92: Relativistic Astrophysics and Particle Cosmology*, ed. C. W. Akerlof & M. A. Srednicki (New York: New York Academy of Sciences), 240
- White, T. R., & Lightman, A. P. 1989, *ApJ*, 340, 1024
- Whitney, A. R., et al. 1971, *Science*, 173, 225
- Wilkins, D. C. 1972, *Phys. Rev. D*, 5, No. 4, 814.
- Williams, R. K. 1991, Ph.D. thesis, Indiana Univ.
- . (Paper 1) 1995, *Phys. Rev. D*, 51, No. 10, 5387
- . 1999, in *The Proceedings of The Eighth Marcel Grossmann Meeting on General Relativity*, ed. T. Piran & R. Ruffini (Singapore: World Science), 416
- . 2001, in *Relativistic Astrophysics: 20th Texas Symposium*, ed. J. C. Wheeler & H. Martel (New York: American Institute of Physics), 448 (astro-ph/0111161)
- . 2002a, *Phys. Rev. D*, submitted (astro-ph/0203421)
- . 2002b, *ApJ*, submitted (astro-ph/0210139)

———. 2003, ApJ, submitted

Williams, R. K., & Eilek, J. A. 2002, in preparation

Williams, R. K., & Hjellming, R. M. (posthumous) 2002, in preparation

Wilms, J., Reynolds, C. S., Begelman, M. C., Reeves, J., Molendi, S., Staubert, R., & Kendziorra, E. 2001, MNRAS, 000, 1 (astro-ph/0110520)

Zdziarski, A. A., & Krolik, J. H. 1993, ApJ, 409, L33

Table 1. Accretion Disk Parameters

Model	α ($\alpha < 1$)	y ($y \leq 1$)	\dot{M} ($\frac{M_\odot}{\text{yr}}$)	M (M_\odot)	r (M)	T^{a} (K)	T_s^{a} (K)	T_e^{b} (K)	T_i^{b} (K)	T_e^{c} (K)	T_i^{c} (K)
1 ^d	0.1	0.3	0.03	10^8	1.3	8.81 (5)	4.13 (6)
2.....	0.1	0.3	0.1	10^8	1.3	8.81 (5)	1.20 (7)	4.53 (8)	2.46 (12)	1.64 (9)	6.79 (11)
3.....	0.1	0.3	0.35	10^8	1.3	8.81 (5)	3.67 (7)	4.19 (8)	6.12 (12)	1.24 (9)	2.07 (12)
4.....	0.1	0.6	0.35	10^8	1.3	8.81 (5)	3.67 (5)	5.93 (8)	4.33 (12)	1.56 (9)	1.64 (12)
5.....	0.1	1.0	0.3	10^8	1.3	8.81 (5)	3.20 (7)	7.72 (8)	3.00 (12)	1.92 (9)	1.21 (12)
6.....	1.0	0.3	0.35	10^8	1.3	4.95 (5)	6.11 (7)	3.63 (8)	3.28 (11)	7.44(8)	1.60 (11)

Additional Accretion Disk Parameters

Model	r(inner) (M)	r(instability) (M)	L_{bol} (erg/s)	L_γ^{b} (erg/s)	L_γ^{c} (erg/s)	β^{e}	h^{a} (M)	h^{b} (M)	h^{c} (M)
1 ^d	1.3 to 150	(does not exist)	3.6 (44)	0.2	0.001
2.....	1.3 to 470	1.089 to 6.73	1.2 (45)	3.0 (42)	2.9 (43)	0.2	0.004	0.587	0.309
3.....	1.3 to 1675	1.089 to 21	4.2 (45)	1.7 (43)	3.5 (43)	0.2	0.013	0.928	0.539
4.....	1.3 to 1675	1.089 to 21	4.2 (45)	2.6 (43)	2.4 (43)	0.2	0.013	0.779	0.481
5.....	1.3 to 1450	1.089 to 17.5	3.6 (45)	2.6 (43)	1.7 (42)	0.2	0.012	0.649	0.413
6.....	1.3 to 2100	1.089 to 55	1.3 (46)	1.3 (44)	2.0 (45)	0.6	0.013	0.215	0.150

^aTemperature (or height) of inner region before instability sets in.

^bAfter instability sets in ($\tau_{\text{es}} < 1$).

^cAfter instability sets in ($\tau_{\text{es}} > 1$).

^dInner region exist; region of instability does not exist.

^e β is the efficiency factor in the bolometric luminosity [it is generally assumed that $0.1 < \beta < 1$ (Eilek 1980)]; $L_{\text{bol}} = \beta(GM/r_{\text{ms}})\dot{M}$.

Table 2: Model Parameters for 3C 279 (PCS)

Case no.	r (M)	E_e (MeV)	$\log(\nu_{\text{ph}})$ (Hz)	$\log(\nu_{\text{peak}})$ (Hz)	$\log(L_{\text{peak}})$ (erg/s)	$\log(L_{\text{obs}})$ (erg/s)	f_1^{a}	f_2
1 ^b	1.089	0.539 ^c	16.23	18.25	46.73	...	4.09 (−2)	1.0
2.....	1.2	0.349	17.5	18.81	46.32	...	4.97 (−2)	1.0
3.....	1.13	0.461	17.5	19.05	46.71	...	4.16 (−2)	1.0
4.....	1.1	0.456	17.5	19.27	47.12	...	4.17 (−2)	1.0
5.....	1.089	0.539 ^c	17.5	19.47	47.46	...	4.09 (−2)	1.0
6.....	1.089	0.539 ^c	18.86	20.21	47.12	...	4.09 (−2)	1.0
7.....	1.089	0.539 ^c	19.56	20.56	46.35	...	4.09 (−2)	1.0
8 ^d	1.089	1.435	18.86	20.61	47.97	46.85	4.09 (−2)	1.0 [0.076]
9.....	1.089	1.838	18.86	20.71	48.39	46.92	4.09 (−2)	1.0 [0.034]
10.....	1.089	2.667	18.86	20.85	48.66	47.06	4.09 (−2)	1.0 [0.025]
11.....	1.089	4.543	18.86	21.06	49.22	47.2	4.09 (−2)	1.0 [0.01]
12.....	1.089	6.433	18.86	21.21	49.54	47.3	4.09 (−2)	1.0 [0.006]
13.....	1.089	11.79	18.86	21.46	50.19	47.5	4.09 (−2)	1.0 [0.002]

^a $\theta_1 = 89^\circ$, $\theta_2 = 91^\circ \Rightarrow \Delta\theta = 2^\circ$.

^bCase numbers 1 through 7 are for PCS by equatorially confined target electrons.

^cWhen the more exact value is used for $r = r_{\text{mb}} = 1.091M$, $E_e \rightarrow 0.512 \text{ MeV} \simeq \mu_e$ (see Paper 1, 2002a; Bardeen et al. 1972), as would be expected for equatorially confined orbits.

^dCase numbers 8 through 13 are for PCS by nonequatorially confined target electrons.

Table 3: Model Parameters for 3C 279 (PPP)

$r = r_{\text{ph}}$ Case no.	$(E_{\mp})_{\text{peak}}$ (MeV)	$\log(\nu_{\text{peak}})$ (Hz)	$\log(L_{\text{peak}})$ (erg/s)	$\log(L_{\text{obs}})$ (erg/s)	$f_1 = f_3^{\text{a}}$	$f_2 = f_4$	f_5
14 ^b	1.289	20.63	46.04	...	1.99 (−2)	1.0	1.0
15.....	174.6	22.59	50.21	47.3	1.99 (−2)	1.0 [0.1]	1.0 [0.122]
16.....	306.7	22.84	50.72	47.25	1.99 (−2)	1.0 [0.06]	1.0 [0.095]
17.....	432.7	23.02	51.07	47.2	1.99 (−2)	1.0 [0.05]	1.0 [0.054]
18.....	711.8	23.21	51.50	47.18	1.99 (−2)	1.0 [0.03]	1.0 [0.053]
19.....	1068	23.40	51.98	47.15	1.99 (−2)	1.0 [0.02]	1.0 [0.037]
20.....	1673	23.60	52.40	47.1	1.99 (−2)	1.0 [0.014]	1.0 [0.026]
21.....	2469	23.77	52.70	47.05	1.99 (−2)	1.0 [0.01]	1.0 [0.022]

^a $\theta_1 = 89.5^\circ, \theta_2 = 90.5^\circ \Rightarrow \Delta\theta = 1^\circ$.

^bCase numbers 14 through 21 have infalling initial (incident) photon frequency, used in the “secondary Penrose Compton scattering” (SPCS), $\nu_{ph} \simeq 7.24 \times 10^{18}$ Hz.

Table 4: Model Parameters for 3C 273 (PCS)

Case no.	r (M)	E_e (MeV)	$\log(\nu_{\text{ph}})$ (Hz)	$\log(\nu_{\text{peak}})$ (Hz)	$\log(L_{\text{peak}})$ (erg/s)	$\log(L_{\text{obs}})$ (erg/s)	f_1^{a}	f_2
1 ^b	1.089	0.539 ^c	16.23	18.24	45.93	...	4.09 (−2)	1.0
2.....	1.099	0.456	17.09	18.91	46.20	46.0	4.17 (−2)	1.0 [0.632]
3.....	1.089	0.539 ^c	17.09	19.11	45.55	46.1	4.09 (−2)	1.0 [0.359]
4.....	1.089	0.539 ^c	17.38	19.37	46.68	46.2	4.09 (−2)	1.0 [0.330]
5.....	1.089	0.539 ^c	17.86	19.72	46.61	46.4	4.09 (−2)	1.0 [0.611]
6.....	1.089	0.539 ^c	18.86	20.21	46.27	...	4.09 (−2)	1.0
7.....	1.089	0.539 ^c	19.56	20.56	45.48	...	4.09 (−2)	1.0
8 ^d	1.089	1.435	18.86	20.61	47.12	46.2	4.09 (−2)	1.0 [0.121]
9.....	1.089	1.838	18.86	20.71	47.54	46.2	4.09 (−2)	1.0 [0.046]
10.....	1.089	2.667	18.86	20.85	47.81	46.1	4.09 (−2)	1.0 [0.020]
11.....	1.089	4.543	18.86	21.06	48.37	46.08	4.09 (−2)	1.0 [0.005]
12.....	1.089	6.433	18.86	21.21	48.69	46.05	4.09 (−2)	1.0 [0.002]
13.....	1.089	11.79	18.86	21.46	49.34	46.08	4.09 (−2)	1.0 [0.001]

^a $\theta_1 = 89^\circ$, $\theta_2 = 91^\circ \Rightarrow \Delta\theta = 2^\circ$.

^bCase numbers 1 through 7 are for PCS by equatorially confined target electrons.

^cWhen the more exact value is used for $r = r_{\text{mb}} = 1.091M$, $E_e \rightarrow 0.512 \text{ MeV} \simeq \mu_e$ (see Paper 1; Williams 2002a; Bardeen et al. 1972), as would be expected for equatorially confined orbits.

^dCase numbers 8 through 13 are for PCS by nonequatorially confined target electrons.

Table 5: Model Parameters for 3C 273 (PPP)

$r = r_{\text{ph}}$ Case no.	$(E_{\mp})_{\text{peak}}$ (MeV)	$\log(\nu_{\text{peak}})$ (Hz)	$\log(L_{\text{peak}})$ (erg/s)	$\log(L_{\text{obs}})$ (erg/s)	$f_1 = f_3^{\text{a}}$	$f_2 = f_4$	f_5
14 ^b	1.289	20.63	45.18	...	1.99 (−2)	1.0	1.0
15.....	6.626	21.21	46.32	46.06	1.99 (−2)	1.0 [0.8]	1.0 [0.859]
16.....	17.28	21.62	47.19	46.1	1.99 (−2)	1.0 [0.4]	1.0 [0.508]
17.....	73.37	22.25	48.58	45.7	1.99 (−2)	1.0 [0.1]	1.0 [0.132]
18.....	106.1	22.37	48.86	45.65	1.99 (−2)	1.0 [0.08]	1.0 [0.096]
19.....	174.6	22.59	49.36	45.6	1.99 (−2)	1.0 [0.05]	1.0 [0.069]
20.....	306.7	22.84	49.86	45.5	1.99 (−2)	1.0 [0.04]	1.0 [0.027]
21.....	432.7	23.02	50.22	45.3	1.99 (−2)	1.0 [0.03]	1.0 [0.014]
22.....	711.8	23.21	50.65	45.25	1.99 (−2)	1.0 [0.022]	1.0 [0.008]
23.....	1068	23.40	51.13	45.2	1.99 (−2)	1.0 [0.015]	1.0 [0.005]
24.....	1673	23.60	51.55	45.0	1.99 (−2)	1.0 [0.009]	1.0 [0.004]
25.....	2469	23.77	51.85	44.8	1.99 (−2)	1.0 [0.008]	1.0 [0.001]

^a $\theta_1 = 89.5^\circ, \theta_2 = 90.5^\circ \Rightarrow \Delta\theta = 1^\circ$.

^bCase numbers 14 through 25 have infalling initial (incident) photon frequency, used in the “secondary Penrose Compton scattering” (SPCS), $\nu_{ph} \simeq 7.24 \times 10^{18}$ Hz.

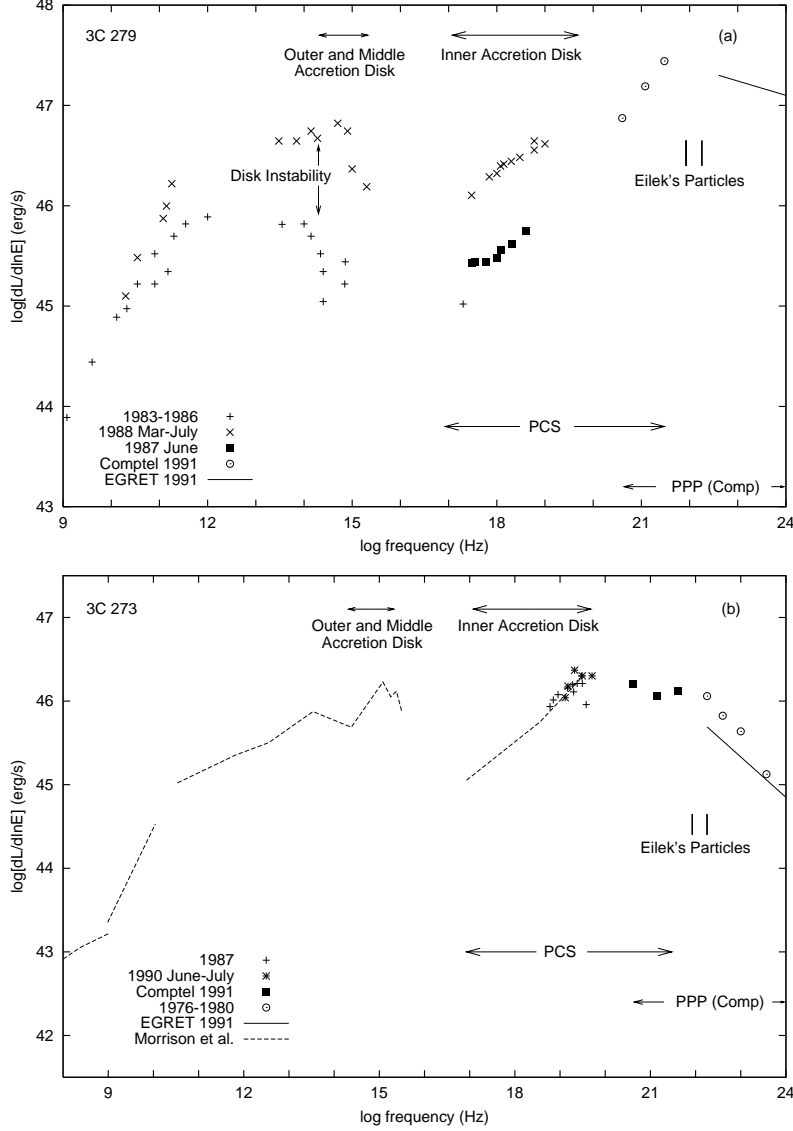


Fig. 1.— Schematic broad-band photon spectra of quasars 3C 279 and 3C 273: comparing observations with theoretical predictions. The intervals indicated by horizontal arrows showing the emission ranges due to Penrose processes [Penrose Compton scattering (PCS) and Penrose pair production (PPP)] are calculated based on a thin disk/ion corona accretion model (see Table 1 and text). General model proposed intervals of accretion disk emission are indicated for a $10^8 M_\odot$ Kerr black hole; only energy intervals of maximum brightness are shown. Eilek’s particle energy locations are indicated by the parallel bars: the higher energy bar indicates the γ -ray emission due to the pion decays ($\pi^0 \rightarrow \gamma\gamma$), peaking at ~ 75 MeV; and the lower energy bar indicates the energy location of the e^-e^+ pairs produced in the subsequent $\gamma\gamma$ pair production of the π^0 -induced photons, peaking at ~ 35 MeV; note, the ordinates and the height of the bars have no meaning (in general $L_\gamma \sim 10^{43}$ erg s $^{-1}$; see text). (a) 3C 279; references for spectral data are given in Hermsen et al. (1993). (b) 3C 273; references for X-ray to γ -ray data are given in Hermsen et al. (1993); spectral data for radio to X-ray frequencies (dashed line) are taken from Morrison, Roberts, and Alberto (1984).

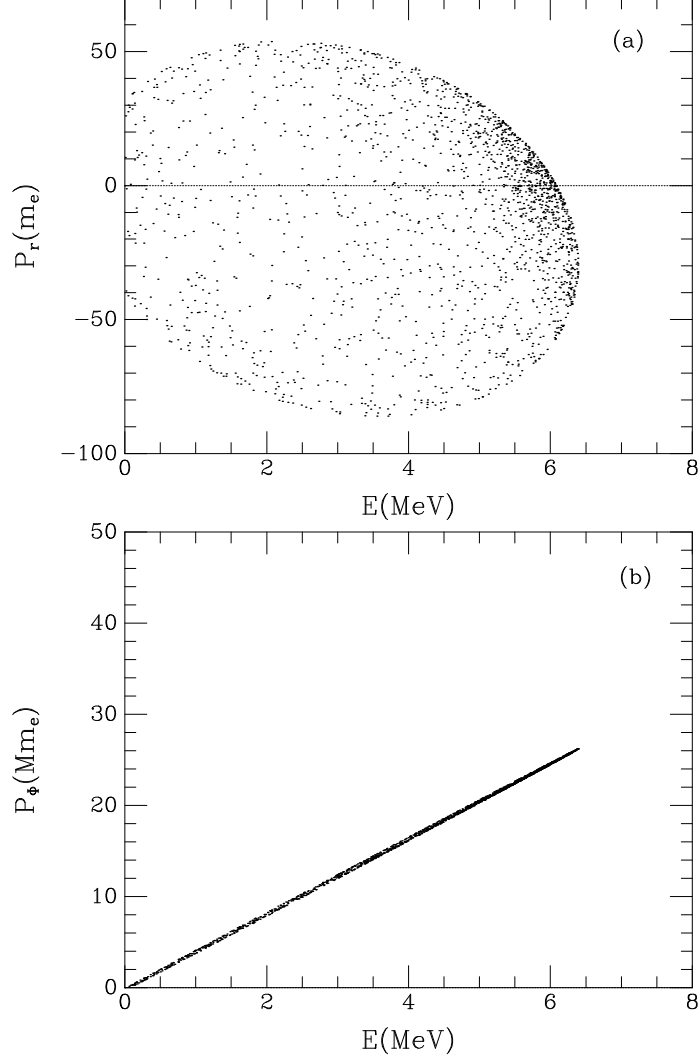


Fig. 2.— Compton scattering at $r_{\text{mb}} \sim 1.09M$: scatter plots showing space momenta of escaping photons scattered by orbiting nonequatorially confined target electrons (each point represents a particle from the 2000 scattering events). Initial and final values are $E_{\text{ph}} = 0.03$ MeV (initial infalling photon), $E_e \simeq 5.93$ MeV (nonequatorially confined target electron), $L_e \simeq 24.1Mm_e$, and $(E'_{\text{ph}})_{\text{max}} \simeq 6.25$ MeV (maximum energy of the escaping final photons). (a) Radial momentum components: $(P'_{\text{ph}})_r$ vs. E'_{ph} . (b) Azimuthal angular momentum components: L'_{ph} vs. E'_{ph} . The units of P_r and $L = P_\Phi$ are m_e and Mm_e , respectively ($G = c = 1$).

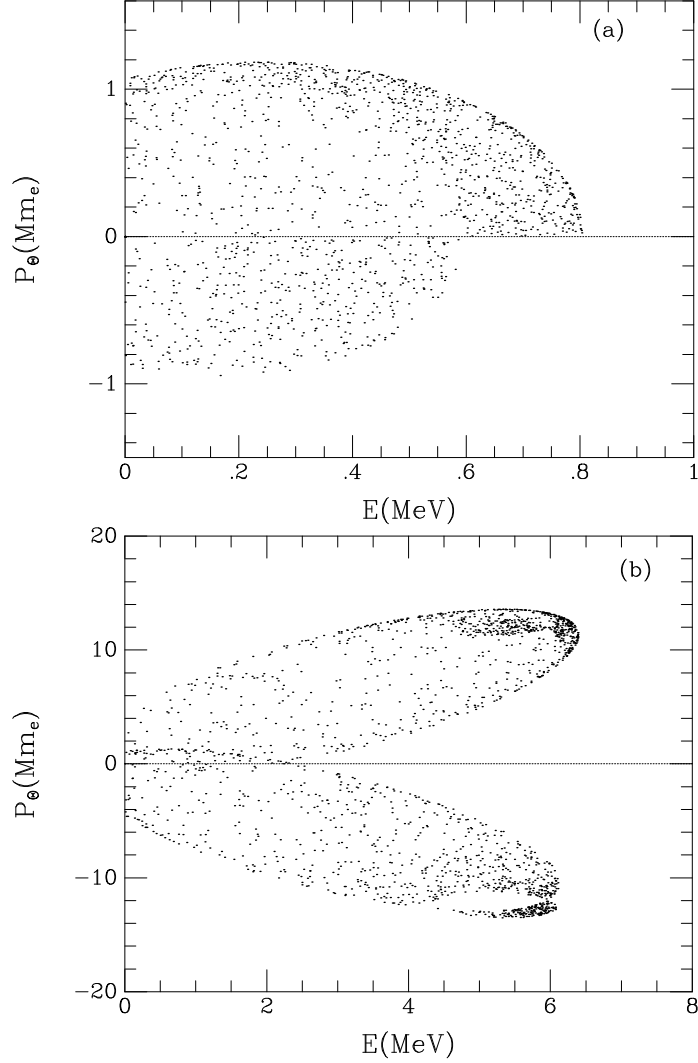


Fig. 3.— Compton scattering at $r_{\text{mb}} \sim 1.09M$: scatter plots showing polar coordinate space momenta for escaping PCS photons, $(P'_{\text{ph}})_\theta \equiv \sqrt{Q'_{\text{ph}}}$ vs. E'_{ph} . (a) $E_{\text{ph}} = 0.03$ MeV, $E_e \simeq 0.539$ MeV (equatorial target electron), $(P_e)_\theta = 0$; $(E'_{\text{ph}})_{\text{max}} \simeq 0.759$ MeV. (b) Same as case presented in Fig. 2 for nonequatorially confined targets, with $(P_e)_\theta \equiv \sqrt{Q_e} = \pm 12.43 Mm_e$ (half are give the positive value, the other half the negative value); plotted here are the corresponding polar momenta.

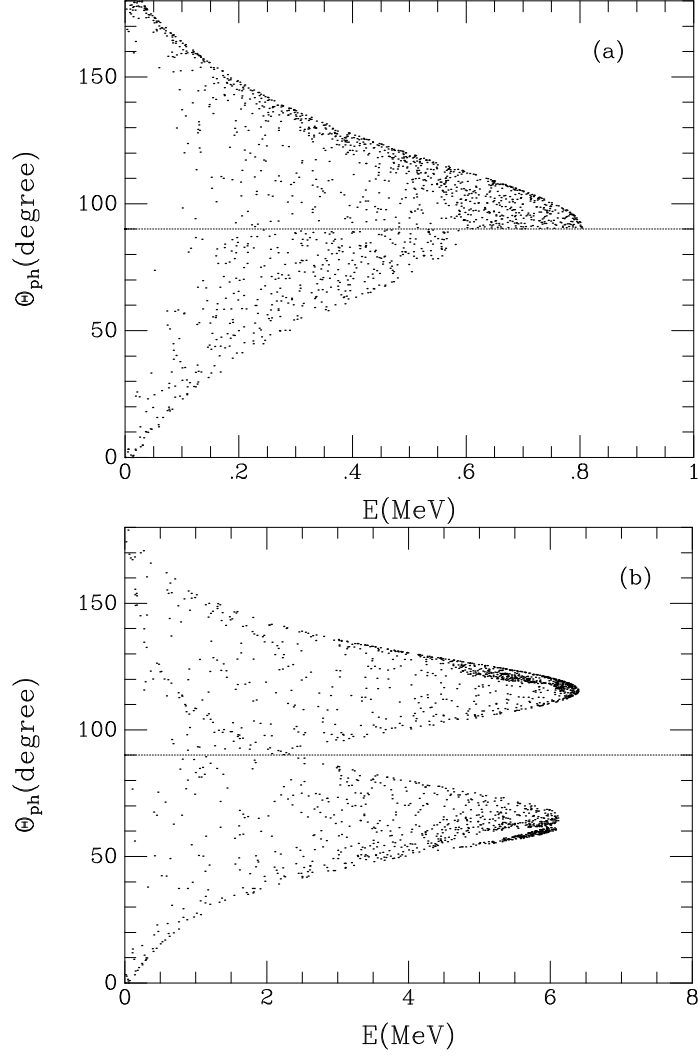


Fig. 4.— Compton scattering: scatter plots displaying polar angles above and below the equatorial plane ($\Theta = 90^\circ$) for escaping photons, Θ'_{ph} (degrees) vs. E'_{ph} . (a) and (b) are the same as cases presented in Figs. 3(a) and 3(b), respectively (compare for corresponding polar coordinate momenta).

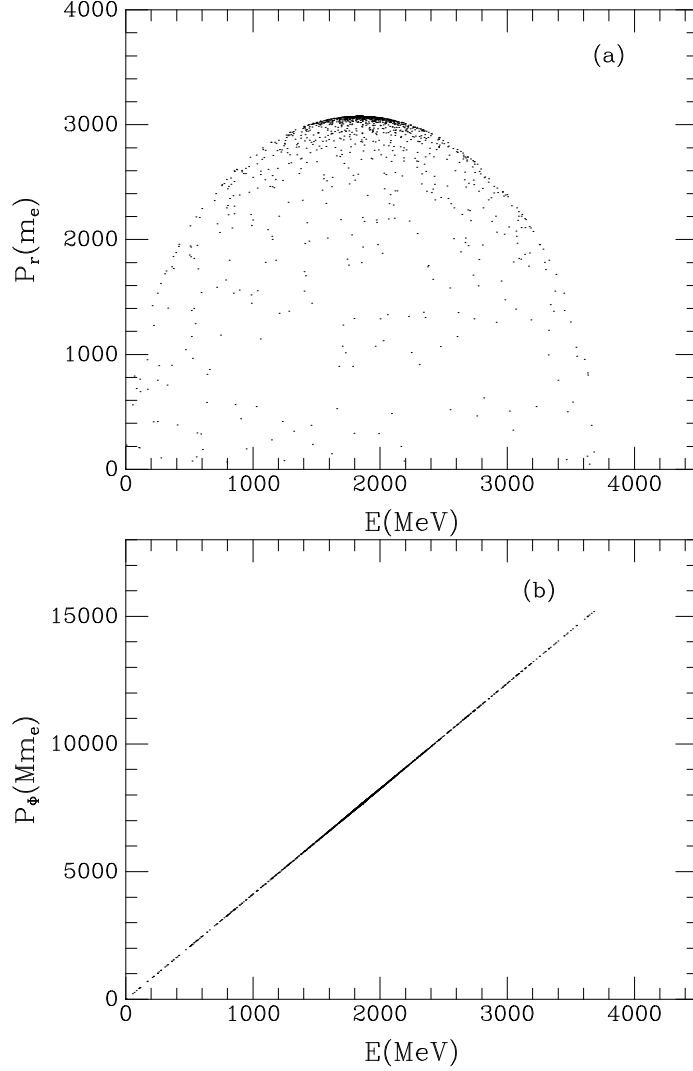


Fig. 5.— Penrose pair production ($\gamma\gamma \rightarrow e^-e^+$) at $r_{\text{ph}} = 1.074M$: scatter plots showing momentum components (each point represents a particle from the 2000 scattering events). For the infalling photons: $E_{\gamma 1} = 0.03$ MeV, and for the target photons: $E_{\gamma 2} \simeq 3.89$ GeV, $L_{\gamma 2} \simeq 1.6 \times 10^4 Mm_e$, with $(P_{\gamma 2})_{\Theta} (\equiv \sqrt{Q_{\gamma 2}}) = \pm 113 Mm_e$; $(E_{\mp})_{\text{max}} \simeq 3.6$ GeV (maximum energy of the escaping pairs). (a) The radial momenta $(P_{\mp})_r$ vs. E_{\mp} . (b) The azimuthal momenta L_{\mp} vs. E_{\mp} . See Fig. 6(c) for the corresponding polar momenta. The units of P_r and L are m_e and Mm_e , respectively ($G = c = 1$).

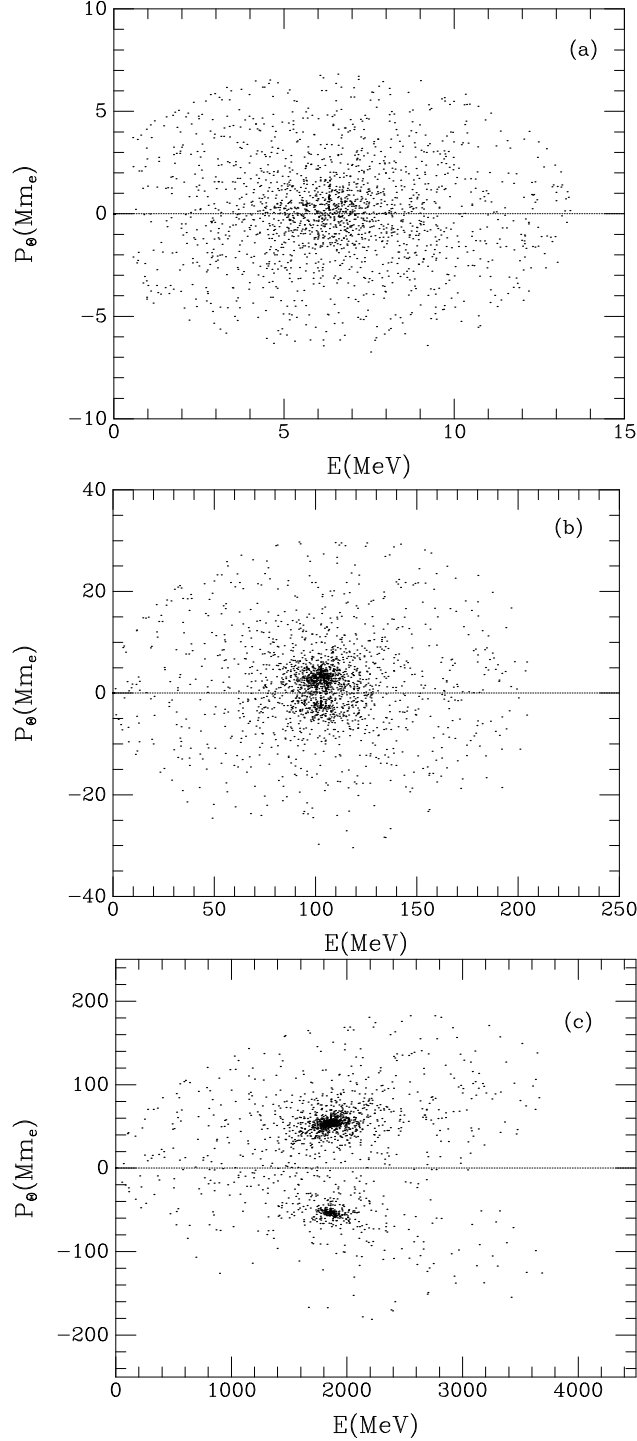


Fig. 6.— Penrose pair production ($\gamma\gamma \rightarrow e^-e^+$): scatter plots showing polar coordinate space momenta for escaping e^-e^+ pairs, $(P_{\mp})_{\Theta} (\equiv \sqrt{Q_{\mp}})$ vs. E_{\mp} . (a) $E_{\gamma 1} = 0.03$ MeV, $E_{\gamma 2} \simeq 13.5$ MeV, $L_{\gamma 2} \simeq 55.6 Mm_e$, with $(P_{\gamma 2})_{\Theta} = \pm 0.393 Mm_e$; $(E_{\mp})_{\max} \simeq 13.34$ MeV. (b) $E_{\gamma 1} = 0.03$ MeV, $E_{\gamma 2} \simeq 207$ MeV, $L_{\gamma 2} \simeq 849 Mm_e$, with $(P_{\gamma 2})_{\Theta} = \pm 6 Mm_e$; $(E_{\mp})_{\max} \simeq 200$ MeV. (c) $E_{\gamma 1} = 0.03$ MeV, $E_{\gamma 2} \simeq 3.89$ GeV; $(E_{\mp})_{\max} \simeq 3.6$ GeV; these are the corresponding polar momenta for Fig. 5.

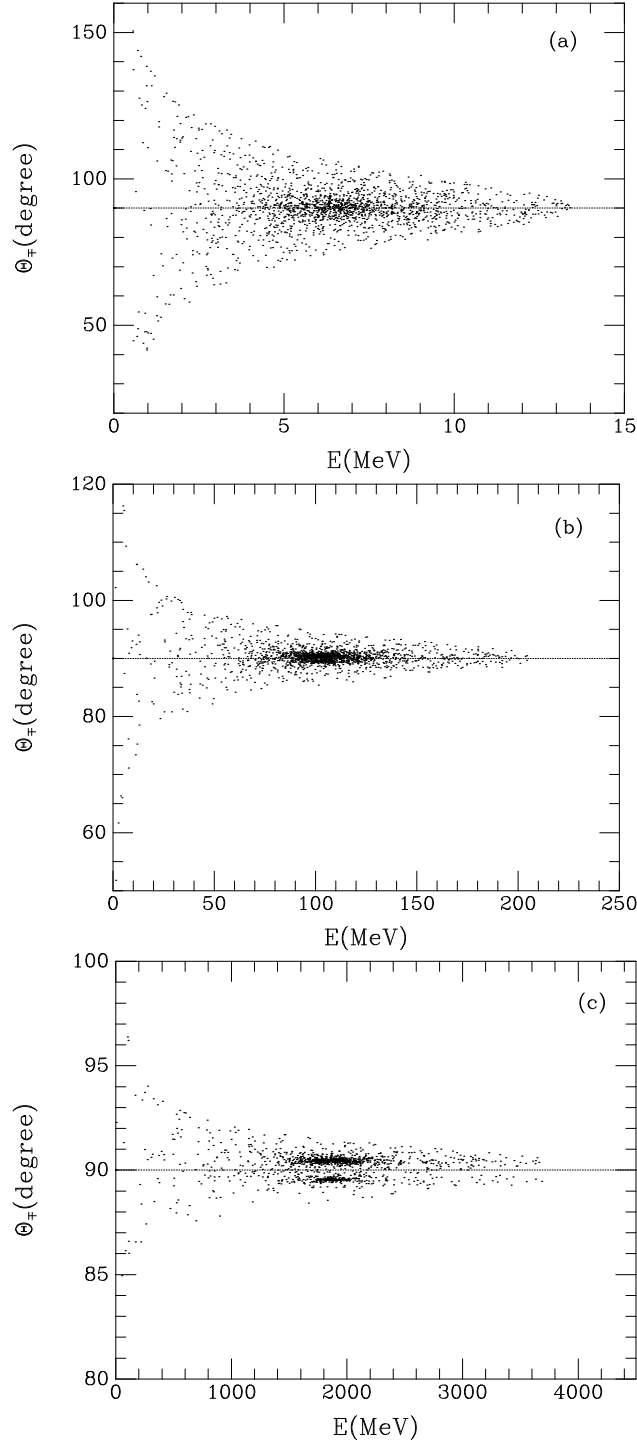


Fig. 7.— Penrose pair production ($\gamma\gamma \rightarrow e^-e^+$): scatter plots displaying polar angles above and below the equatorial plane ($\Theta = 90^\circ$) for escaping e^-e^+ pairs, Θ_{\mp} (degrees) vs. E_{\mp} . (a), (b), and (c) are the same as cases presented in Figs. 6(a), 6(b), and 6(c), respectively (compare for the corresponding polar coordinate momenta).

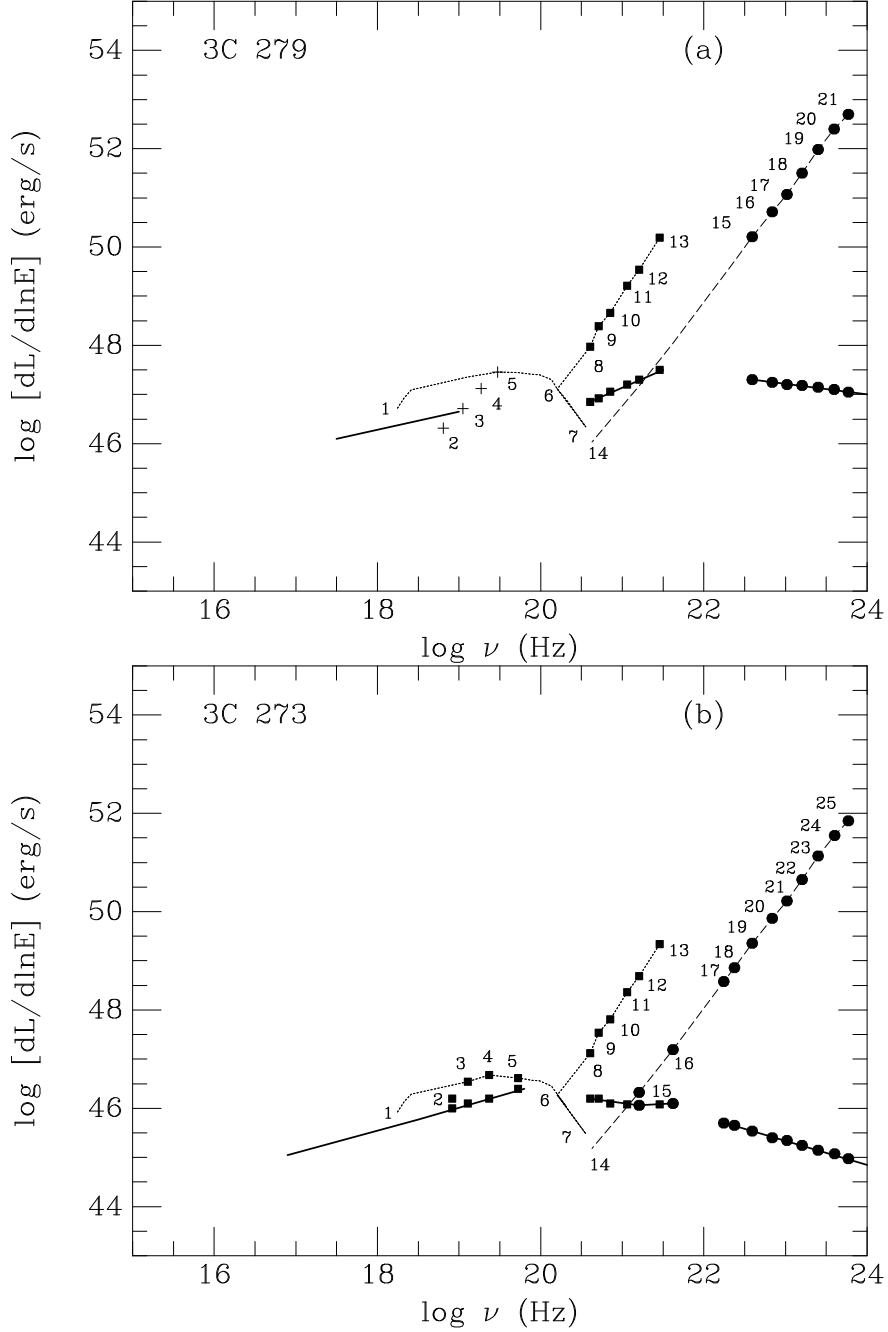


Fig. 8.— Comparing the theoretical spectra with observations for 3C 279 and 3C 273. The calculated PCS and PPP ($\gamma\gamma \rightarrow e^-e^+$) luminosity spectra are represented by the solid squares and large solid dots, respectively. The observed spectra is indicated by the solid line. The upper curves with the solid squares and solid dots superimposed on the dotted line and the dashed line, respectively, for PCS and PPP, are the spectra calculated from this model. Superimposed on the lower solid line of the observations are solid squares and solid dots from the model calculations that have been adjusted to agree with observations. These adjustments depend on the fraction of particles that actually undergoes scattering events. This fraction is defined by the f_n parameters. The numbers on the figures correspond to the case numbers on Tables 2 through 5 (see text for further details). (a) Spectra for quasar 3C 279. (b) Spectra for quasar 3C 273.